Western 🛡 Graduate&PostdoctoralStudies

Western University
Scholarship@Western

Electronic Thesis and Dissertation Repository

7-26-2018 2:00 PM

A Composite Material-based Computational Model for Diaphragm Muscle Biomechanical Simulation

Brett Coelho
The University of Western Ontario

Supervisor
Samani, Abbas
The University of Western Ontario

Follow this and additional works at: https://ir.lib.uwo.ca/etd

🎨 Part of the Biomechanical Engineering Commons

Abstract

Lung cancer is the most common cause of cancer related death among both men and women. Radiation therapy is the most widely used treatment for this disease. Motion compensation for tumor movement is often clinically important and biomechanics-based motion models may provide the most robust method as they are based on the physics of motion. In this study, we aim to develop a patient specific biomechanical model that predicts the deformation field of the diaphragm muscle during respiration. The first part of the project involved developing an accurate and adaptable micro-to-macro mechanical approach for skeletal muscle tissue modelling for application in a FE solver. The next objective was to develop the FE-based mechanical model of the diaphragm muscle based on patient specific 4D-CT data. The model shows adaptability to pathologies and may have the potential to be incorporated into respiratory models for the aid in treatment and diagnosis of diseases.

Keywords

Co-Authorship Statement

This thesis has been written by Brett Nelson Coelho under the supervision of Dr. Abbas Samani. The research presented has been conducted by the principal author and guided by the thesis supervisor.

The material presented in Chapter 2 is entitled "A micro to macro mechanical approach for skeletal muscle tissue mechanical characterization." It was authored by B. N. Coelho and A. Samani and has been submitted to the Journal of the Mechanical Behavior of Biomedical Materials.

The material presented in Chapter 3 is entitled "Micromechanics Based Modelling of in-vivo Respiratory Motion of the Diaphragm Muscle." It was authored by B. N. Coelho and A. Samani.

Acknowledgments

Table of Contents

List of Tables

List of Figures

We used data we generated from the ECM simulation in the previous part to construct FE model of normal skeletal muscle. Using this model, uniaxial extensions of the constructed skeletal muscle tissue model were simulated in fiber and across fiber directions. Resulting stress-strain relations are illustrated in Figure 2-5(a) and (b) that demonstrate the data in fiber and cross fiber directions, respectively. These figures also show corresponding experimental stress-strain data of fresh porcine skeletal muscle as reported by Takaza et al[19]. Ad-hoc optimization of Z-disc in the model led to a Neo-Hookean hyperelastic parameter C_1 value of 15 MPa. This may be regarded as the first estimate of hyperelastic parameter of intact *ex vivo*

As aforementioned, discrepancies exist among stress-strain data obtained by different investigators for skeletal muscle tissue in fiber and cross fiber directions. However, it has been consistently shown that the cross-fiber direction exhibits a stiffer and generally more linear trend in the case of experimental testing on fresh and *in-vivo* tissue samples[54,52,16,20]. The following Figure 2-6(a) and (b) are extensions of Figure 2-5(a) and (b) to include the fittings obtained based on the strain energy density equation introduced in Section 2.5. While Jenkyn et al. fit the model to rabbit experimental data we used our simulation data to determine the model's coefficients. Disparities seen between researcher's experimental data are not uncommon, Takaza and Nie porcine experimental data have been found to mainly disagree in the along fiber direction, which are expected to be due to experimental protocol. The dynamic high strain rate testing used by Nie may have accelerated the process of rigor-mortis which has been shown to increase the stiffness and linearity of the tissue mechanical behaviour in the along the fiber direction[20]. The results from Jenkyn et al. are shown because their works used data collected from *in vivo* experiments on rabbits to determine the muscle tissue anisotropic hyperelastic parameters. The coefficients we determined based on our simulation seen in Table 2-4 are compared to that of the work performed by Jenykns et al. and Linden. The constants a1 and a2 describe the passive stiffness in the perpendicular and parallel fiber directions, respectively. The elevated stiffness transverse to fibers is reflected

List of Abbreviations

3D   Three Dimensional

EBRT External Beam Radiation Therapy

ECM Extra Cellular Matrix

CT   Computed Tomography

4D CT Four-Dimensional Computed Tomography

HU   Hounsfield Unit

FE   Finite Element

FEM   Finite Element Analysis

FFD   Free Form Deformation

ITK   Insight Toolkit

ICP   Iterative Closest Point

Chapter 1

1 « Introduction »

1.1 « Background and Motivation »

The diaphragm muscle is a fundamental organ which helps pumping air in and out of the lungs and ultimately allows for sufficient oxygen exchange into the blood stream. Respiratory motion is a complex phenomenon driven majorly by diaphragm muscle contraction in conjunction with the intercostal muscles contraction. It is expected that biomechanical modelling of the diaphragm muscle will be a useful tool for understanding the physiology of the respiratory system and the diagnosis and treatment of related diseases. Among others, lung cancer has not only proven to be the deadliest respiratory disease but also the deadliest cancer type. According to the American Cancer Society about 14% of all new cancers are lung cancers. It is by far the leading cause of death, more people die of lung cancer than colon, breast, and prostate cancers combined. A highly common treatment technique for lung cancer involves external beam radiation therapy (EBRT), which aims a radiation beam at the lung tumour in an attempt to destroy the cancerous cells in the tumour. A serious issue with this technique is that tumour motion is generally clinically significant[1] and without accurate tumour motion tracking during breathing, healthy tissue is irradiated along with the tumor tissue, which could consequently severely degrade the effectiveness of the treatment. When tumour motion is deemed clinically significant the methods used to compensate for this motion include motion encompassing methods, respiratory gating, breath-hold techniques, and real-time tumour tracking. Motion encompassing methods irradiate a large volume of tissue compared to the tumour volume, which can significantly damage healthy tissue. Respiratory gating involves irradiation during only a specific portion of the breathing cycle, this serves to minimize healthy tissue damage, however, it also leads to extended treatments times. Breath-hold techniques attempt to immobilize tumour motion to facilitate tumour irradiation, however, most lung cancer patients experience weakened pulmonary function

and this technique may not be feasible. Real-time tracking methods involve dynamically adjusting the radiation beam to follow the tumour's position. If idealized, real-time tracking methods could provide the most efficient method for treatment, although in its current state, accurate tumour motion/deformation prediction in real time remains an issue. Direct tracking methods include X-ray fluoroscopy or the implant of a miniature RF coil, both of which having their associated risks due to additional imaging radiation and invasiveness, respectively. Indirect tracking methods include correlating internal and external organ motions, often using chest motion data as the external signal to determine internal organ motion. Internal organ motion can be predicted based on image segmentation/association or biomechanical respiratory modelling. As our physiological understandings and computational techniques improve, the latter may provide more accuracy[2,3,4]. A major component of a biomechanical model of the respiratory system is the lung-diaphragm boundary conditions. Most have taken the approach of image registration to determine the deformations of the lower boundary of the lung through non-rigid registration techniques. Unfortunately, because of lack of sufficient CT image contrast and the diaphragm's large deformation, non-rigid registration techniques can lead to inaccuracies in predicted deformation fields. The focus of this thesis is developing a patient specific biomechanical model of the diaphragm in order to predict its deformation field during respiration. This research also serves to provide insight into muscle tissue modelling, the mechanical effects of pathologies, and to predict the contraction forces of the diaphragm muscle.

1.2 « Anatomy, Microstructure, Physiology, and Pathology »

The diaphragm is a musculotendinous sheet that lies directly beneath the lungs with two major lobes that serve to expand the lung during contraction. Among healthy humans, the muscle thickness tends to vary between 4-5 mm in thickness[5]. The inferior borders of the diaphragm attach tendonously to the lower ribs, lower lumbar vertebrae, arcuate ligaments, and the sternal xiphoid process. During respiration, the diaphragm muscle contracts in conjunction with the surrounding intercostal muscles, which serve to expand the rib cage. Found almost directly in the center of the diaphragm, but positioned slightly posteriorly, the tree foil shaped central tendon of the muscle can be found. Average measures among

adult humans predict a tendon with an area of approximately 143 centimetres squared[6,7,5]. The diaphragm has two domes that are essentially innervated separately each by a phrenic nerve[8,9]. The right dome is generally superior to the left due to the presence of the liver and heart. The larger right lobe of the liver lies beneath the right hemi diaphragm dome and the heart is positioned above the left dome[10]. The diaphragm's muscle is a high endurance skeletal muscle, and compared to most skeletal muscles, it differs slightly such that it favours more slow twitch muscle fiber with a distribution of ~60% slow and 40% fast twitch fibers[11,12]. The muscle fibers of the diaphragm emerge from their peripheral attachments and attach to the central tendon, which generates essentially a radial pattern along the curved surface of the muscle[13]. Figure 1-1(a) shows a cadaveric specimen of a human diaphragm which demonstrates the muscle fibers and their configuration. Skeletal muscle is comprised of multiple bundles of muscle fiber cells which contain myofibrils. Myofibers are made up of repeating units of sarcomeres where actin and myosin filaments are attached to structurally important Z-disks that are oriented perpendicular to the fiber direction. The muscle fibers are the contractile units of muscle, as they contract, Z-disks move closer together. Muscle tissue is majorly comprised of these myofiber bundles found within a sarcolemma sheath which provides further structural support. Figure 1-1(b) shows an electron micrograph of skeletal muscle tissue where myofibers and Z-disks are apparent. Mitochondrion, collagen, and fat are also present both inside muscle cells and in the extracellular matrix known as intra and extra myocellular. The volume percentages of each of these components varies from person to person depending mainly on their exercise level, age, and any underlying pathologies[14,15,16,17,18]. Pathologies can affect muscle functionality through both microstructural changes as well as neurological function, essential for activation. Fibromyalgia is one such disease that has been found to effect the microstructure of skeletal muscles, including reports of reduced collagen content, increased lipid droplets, and altered mitochondrial density[19,20]. Muscle spasticity also negatively effect muscle both functionally and structurally[21]. On the other hand, unilateral paralysis, which often occurs in conjunction with lung tumours, is a result of loss of phrenic nerve signaling leading to partial or no contraction in one of the hemi diaphragm domes. The progression of the disease is marked by ballooning of the affected hemi diaphragm into the lung and difficulty breathing[22,23,23].
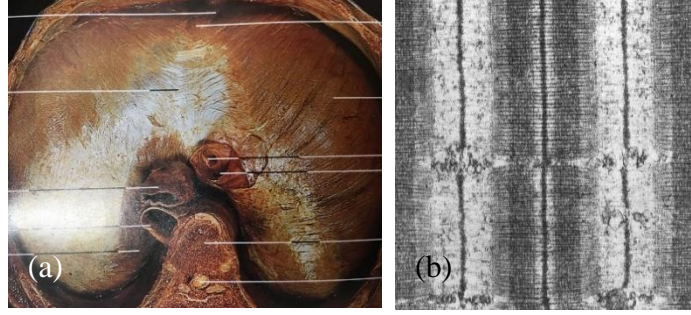
Figure 1-1 (a) a cadaveric diaphragm muscle showing muscle fiber arrangement[6], and (b) a skeletal muscle tissue electron micrograph with myofibrils oriented horizontally and vertical Z-disks structures[24]. (a) and (b) reproduced with permission.

1.3 « Theory »

1.3.1 Elasticity and Hyperelasticity

The Elastic theory is specific towards the deformation of elastic materials. It relates externally applied forces to the material to its deformations according to its mechanical properties. Elastic materials return to their initial shape and size after removing forces that cause the material to deform. In its simplest form, materials are described as linearly elastic, which describes the relationship between the stress and strain. This relationship is known as Hooke's law which can be stated in the form of stress (σ) strain (ε):

$$\sigma = E\varepsilon \tag{1}$$

Hyperelastic models are constitutive models developed such that the stress-strain relationship is derived from the strain energy density function. The main reason for their development is that linear elastic models do not accurately describe observed material mechanics, especially when large deformations are involved. Hyperelasticity provides a means of modelling the stress-strain relationship of materials that can be defined as non-linearly elastic, isotropic, and generally independent of strain rate. The two major sources of nonlinearity arise from the intrinsic mechanical properties of constituents and geometric nonlinearity; which pertains to a change in material stiffness due to a change in its

geometry. Several hyperelastic models have been introduced to model various materials including biological tissues. For the purpose of this thesis, Neo-Hookean and Yeoh models are considered for incompressible materials. The hyperelastic model for a three-dimensional incompressible neo-Hookean material has a strain energy density function that follows:

$$W = C_1 (I_1 - 3) \tag{2}$$

where C_1 is a material constant and I_1 is the first invariant of the Cauchy-Green deformation tensor such that

$$I_1 = \lambda_1{}^2 + \lambda_2{}^2 + \lambda_3{}^2 \tag{3}$$

λi's are the principle stretches. The Yeoh model has been widely used for the modelling of soft tissues of the human body[25,26], which are known to be nearly incompressible and nonlinear elastic. The Yeoh model is another commonly used model which includes 3 terms as follows:

$$\sum_{i=1}^{3} C_i (I_1 - 3)^i \tag{4}$$

Where the Ci's are material constants often referred to as hyperelastic parameters. Another hyperelastic model that is used in this research is the Ogden model which follows:

$$\sum_{i=1}^{N} (\frac{\mu_i}{\alpha_i} (\lambda 1^{\alpha_i} + \lambda 2^{\alpha_i} + \lambda 3^{\alpha_i} - 3)) \tag{5}$$

where α_i and μ_i are hyperelastic coefficients, and λi's are the principle stretches. Again, this model is widely used to model biological tissue, including human tissue[27,28,29]. Hyperelastic parameters for such models are determined based on stress-strain experimental data.

1.3.2   Image Segmentation

Image segmentation is a major component for developing and validating the proposed diaphragm biomechanical model. In order to attain the patient specific model's geometry, the diaphragm is segmented based on a previously developed fully automatic segmentation method for the human diaphragm in non-contrast CT images[30]. The technique is capable of segmenting the whole diaphragm using conventional CT images of the thorax where image contrast around the diaphragm area is very low. It uses thresholding, connected component analysis, a priori of knowledge about the diaphragm, and a B-spline filter. The method was refined manually to ensure precise differentiation between the heart and diaphragm, a region where contrast is generally low with CT images. In addition to diaphragm segmentation, the ribs were segmented by thresholding the CT images at ~ 150 HU, their locations during respiration are indicative of thorax expansions. Figure 1-2 shows examples of diaphragm muscle volume, diaphragm muscle surface, and rib segmentations in 4D CT for a patient in respective panels (a), (b), and (c). The diaphragm muscle volume in Figure 1-2(a) is shown as a dark mass and overlaid with its corresponding 4D CT image. Figure 1-2(b) and (c) display a slice of the diaphragm muscle surface and rib segmentation in white. All segmentation techniques were implemented in ITK and inspected in 3D slicer where minor manual edits were applied to improve segmentation quality.
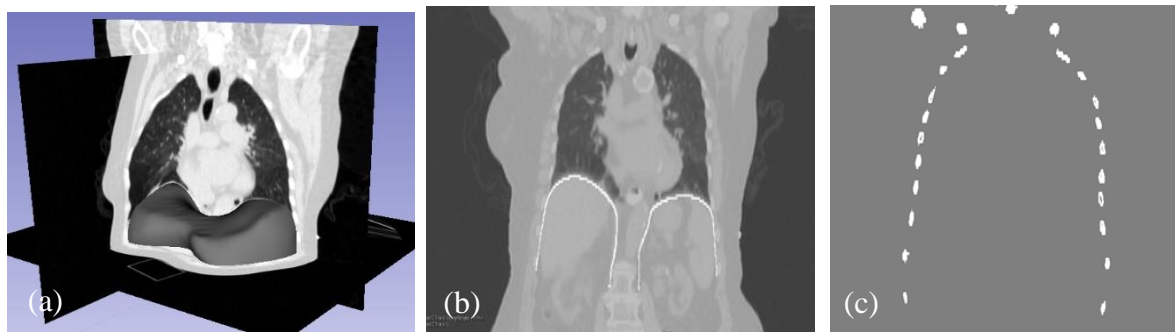
Figure 1-2 (a) Segmented diaphragm volume overlaid with 4D CT data (dark central mass (b) Segmented diaphragm muscle surface in white overlaid with 4D CT data (contract muscle configuration) (c) Segmented ribs.

1.3.3   Image Registration: Rigid and non-Rigid

The Image registration involves transforming different data sets into a single coordinate system. An important feature of the proposed model are its boundary conditions. The diaphragm attaches to the lower ribs, sternum, and intercostal muscles which can be segmented in CT images. The rib cage and intercostals can be segmented at both end exhalation (rest state) and end inhalation for each set of CT images. Rigid registration is the simplest form of image registration which can be used to determine the displacement field of the ribs from end exhalation to end inhalation. The ribs are significantly stiffer than surrounding tissues making rigid registration an appropriate choice for determining their motion throughout respiration since their geometry remains essentially unchanged. The technique aligns each corresponding rib feature at different respiratory phases in order to predict their displacement.

Next, non-rigid registration with free form deformation (FFD) was used to elucidate the motion of the intercostal muscles between similar respiration phases. The intercostal muscles are a softer tissue found surrounding the ribs and diaphragm. This technique applies a grid to an image and iteratively minimizes an image similarity metric (NMI) between two images as it defines a geometric mapping between the coordinates of both images. Once minimized, the solution converges to the smoothest and most accurate predicted deformation field given the inputs provided. The deformation fields acquired pertaining to the ribs and intercostals were important pertaining to areas that interface with the diaphragm and its peripheral attachments. Image segmentation and registrations techniques were implemented in ITK.

1.4   « Literature Review »

1.4.1   Mechanical Modelling of Skeletal Muscle Tissue: Passive and Active

The function of muscle tissue is contraction towards motion generation. Skeletal muscle is characterized by both its passive mechanical properties and active response. The passive

behavior of skeletal muscle tissue has two major features including hyperelasticity and transverse isotropy[31]. Hyperelasticity models the non-linear stress-strain relationship and transverse isotropy refers directional mechanical properties; specifically, when forces are applied along and transverse to the muscle fiber direction found in the muscle tissue. The myofibers behave both passively and actively whereas the extracellular matrix only behaves passively. Based on the aforementioned description of muscle tissue, models have been proposed for simulating its mechanics. The Hill's model is the most renowned model which includes active, passive and elastic elements. The active and elastic elements work in series while passive component is parallel as seen in Figure 1-3.
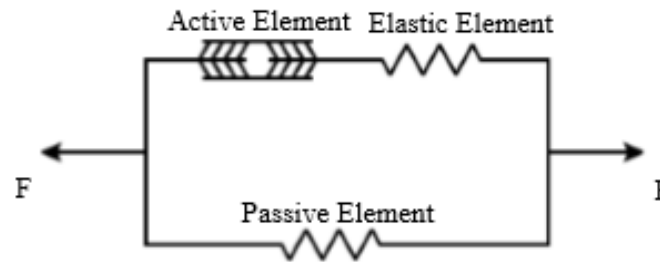
Figure 1-3 Hill's model for muscle tissue mechanical modelling.

The model generates internal stress through the active element which leads to contraction of both the active and passive components due to bonding. The passive stresses are distributed in both the myofiber and extracellular matrix parts. In skeletal muscles active contraction requires nerve stimulations and depends on the parameters such as the velocity of contraction, thermal energy loss, and the current sarcomere length related to its rest length. The muscles can contract eccentrically, concentrically, and isometrically following an approximated force-length relationship that can be elucidated with experimental work (e.g. tetanized muscles in baboons). Unlike most skeletal muscles, the diaphragm better approximates isometric contractions allowing for a more consistent contraction force with respect to the force development over time. The expansion of the rib cage pulls the muscle periphery in an outward and upward fashion during contraction which serves to maintain sarcomere length[32]. Our proposed model follows a finite element (FE) approach inspired by the Hill's model. This FE is implemented in an off-the-shelf solver Abaqus (Dassault

Systèmes Simulia Corp., Providence, RI, USA). In this model the muscle tissue is modelled as a composite material with the extracellular matrix (ECM) representing the background material housing the myofibers which have different mechanical properties. In the proposed model rebars, which mimic the myofibers, are embedded into elements representing the ECM to model skeletal muscle. Contractions are assumed to be isometric, and prestresses are applied to rebars increasing linearly to a maximum contraction force. This composite model leads to a self-contained anisotropic behavior. Groups who model skeletal muscle generally develop in-house computer programs for modelling the transverse isotropy for skeletal muscle tissue. Among more recent works, Zhang et al. used an extension of the Hill's model to simulate skeletal muscle contraction, containing passive elements (PE), active/contractile elements (CE), and elastic elements (EE). The muscle force F is a sum of the forces in the elements where

$$F = \mathrm{F}^{PE} + \mathrm{F}^{EE} = \mathrm{F}^{PE} + \mathrm{F}^{CE} \tag{6}$$

which is analogous to the nominal stresses along the fiber direction. The passive stress T^{PE} is defined as:

$$T^{PE} = T_0^M f_{PE}(\lambda_f) \tag{7}$$

Where T_0^M denotes the maximal muscle nominal stress which determines the maximal muscle contraction force and λ_f is the stretch ratio in the fiber direction. The passive force-length relation of the passive element f_{PE} is given by:

$$f_{PE}(\lambda_f) = 2aA(\lambda_f - 1)e^{a(\lambda_f - 1)^2}, \text{for } \lambda_f > 1 \tag{8}$$

Where A and a are material constants and $f_{PE} = 0$ if λ_f is not greater than 1. The active stress T^{CE} is given by:

$$T^{CE} = T_0^M f_{CE}(\lambda_f)\alpha(t)\gamma$$

where γ is the activation level of the muscle from 0 to 1, α represents the time dependence of the activation, and $f_{AE}(\lambda_f)$ is the active force-length relation in the active element.

According to experimental data from an adult baboons[33], the force-length relationship of the diaphragm muscle is

$$f_{\text{CE}}^{Dia}\left(\lambda_f\right) = \begin{cases} 1.80\lambda_f - 0.80, & \text{for } 0.6 \leq \lambda_f < 0.7 \\ 2.37\lambda_f - 1.20, & \text{for } 0.7 \leq \lambda_f < 0.8 \\ 1.61\lambda_f - 0.59, & \text{for } 0.8 \leq \lambda_f < 0.9 \\ 1.42\lambda_f - 0.42, & \text{for } 0.9 \leq \lambda_f < 1.0 \\ -0.55\lambda_f + 1.55, & \text{for } 1.0 \leq \lambda_f < 1.1 \\ -2.11\lambda_f + 3.27, & \text{for } 1.1 \leq \lambda_f < 1.2 \\ 0, & \text{otherwise} \end{cases} \tag{9}$$

The time dependence of the muscle activation α(t) was fitted to experimental data obtained from dogs[34].

1.4.2 Modeling of Diaphragm Muscle Tissue Passive Mechanical Properties

The passive mechanical properties of various constituents of skeletal muscle tissue is highly important for the implementation of our proposed model[12,35,36,37,38,39]. Experimental testing to determine the stress-strain relationship of a material is a traditional method for mechanical modelling. Stress-strain data obtained from the experimental testing is then used for fitting to a constitutive model, such as the hyperelastic models described in section 1.3.1. In this investigation, we use an alternate approach where the muscle tissue modelling is based on a micro-to-macro mechanical approach described in Chapter 2. The mechanical properties for myofiber bundles, mitochondria, fat, and collagen are attained from literary experimental data. As aforementioned, the volume percentages of the micro constituents found in muscle tissue are variable, and therefore the model mechanics are adaptable to encompass such variability since the overall mechanics of the tissue is a combination of the mechanics of its constituents. The micro-to-macro technique follows a structural approach for modelling muscle tissue, where the tissue if broken down into its major constituents. Their volume percentages and distribution throughout tissue determine the overall mechanical characterization of the tissue. Mathematical modelling using strain

energy density equations is also popular to represent the passive mechanics of skeletal muscle tissue[28,40,41,42]. An existing hyperelastic model used by Jenkyn et al. and Linden is an extension of the Fung hyperelastic model whose parameters determine strain energy density in the tissue, which are found experimentally[28,43,41]. The anisotropic strain energy density equations representing these models are as follows:

$$W^{\text{parallel}}(e_2) = \frac{k}{a_2}(e^{a_2 e_2} - a_2 e_2) \qquad (10)$$

$$W^{\text{perpendicular}}(e_1) = \frac{k}{a_1}(e^{a_1 e_1} - a_1 e_1) \qquad (11)$$

where a_1 and a_2 are hyperelastic parameters that relate to the passive stiffness in cross-fiber and fiber direction, respectively. Their work includes a shear component, however, it was independent of the above equations and not analyzed in our research.

1.4.3 Diaphragm Muscle Contraction Modeling Using Strain Energy Density Approach

Existing models that simulate diaphragm muscle contraction can be scarcely found in the literature. The major components presented by Zhang et al. follow an incompressible hyperelastic transversely isotropic model proposed by Martins et al. where the Hill's model is extended into 3 dimensions[32,44]. The contraction model was presented in Section 1.4.1. After determining the active and passive stresses presented in Section 1.4.1, followed by integration related to fiber stretches, the muscles were modelled using strain energy density equations as follows:

$$U_I = ce^{b\left(\bar{I}_1^C - 3\right) - 1} \qquad (12)$$

$$U_f\left(\bar{\lambda}_f, \alpha, \gamma\right) = U_{\text{PE}}\left(\bar{\lambda}_f\right) + U_{\text{CE}}\left(\bar{\lambda}_f, \alpha, \gamma\right) \qquad (13)$$

where U_I and U_f are the strain energies stored in the isotropic hyperelastic matrix and muscle fibers, respectively. c and b are material constants. Our proposed model is also founded on Hill's model concept; however, the muscle tissue intrinsic mechanics is

modelled based on an adaptable micro-to-macro composite material approach we developed for skeletal muscle tissue as presented in Chapter 2. In order to simulate contraction, Zhang et al. used force-velocity experimental data measured on the diaphragm muscle of a single adult baboon[33]. Their model involves contraction of the intercostal muscles in the thorax. They explained that the muscle fiber installations were done according to a radial pattern from the central tendon to the bottom edge. In their model, they included linear variations of abdominal and pleural pressures that were applied to the lower diaphragm surface and inner thorax, respectively. They used ranges of 0 to 2 kPa and −0.5 to −0.75 kPa during normal quiet breathing for these surfaces, respectively.

1.4.4   Objectives

The overarching objective of this work is to develop a patient specific biomechanical model of the diaphragm to simulate contraction in normal and pathological diaphragms. The model is developed such that it can be integrated into a respiratory system model, including the lung, to model lung tissue deformation throughout the respiration cycle. A micro-to-macro mechanical approach is used to accurately characterize the intrinsic mechanics of the skeletal muscle tissue with a structural approach. This proposed approach allows adaptability to a broad range of healthy and pathological diaphragmatic muscle tissue while it enables exploring the sensitivity of the tissue mechanical properties to microstructural and pathological changes. Another objective of the work is to estimate the contraction forces found within the diaphragm muscle. To achieve this objective an inverse problem framework which utilizes optimization was developed with the diaphragm mechanics model used as the forward model. Given its utility as a forward model, the diaphragm model should be computationally efficient, robust and implementable using an off-the-shelf FE software package. The latter is important for availability to the research community.

1.5 « References »

1. Wang Y, Bao Y, Zhang L, et al. Assessment of respiration-induced motion and its impact on treatment outcome for lung cancer. *Biomed Res Int*. 2013;2013:872739. doi:10.1155/2013/872739

2. Gaede S, Lee T-Y, Samani A, Karami E. A machine learning approach for biomechanics-based tracking of lung tumor during external beam radiation therapy. In: Webster RJ, Fei B, eds. *Medical Imaging 2018: Image-Guided Procedures, Robotic Interventions, and Modeling*. Vol 10576. SPIE; 2018:39. doi:10.1117/12.2293841

3. Fassi A, Schaerer J, Fernandes M, Riboldi M, Sarrut D, Baroni G. Tumor Tracking Method Based on a Deformable 4D CT Breathing Motion Model Driven by an External Surface Surrogate. *Int J Radiat Oncol*. 2014;88(1):182-188. doi:10.1016/j.ijrobp.2013.09.026

4. Karami E. A biomechanical approach for real-time tracking of lung tumors during External Beam Radiation Therapy (EBRT). *Electron Thesis Diss Repos*. August 2017. https://ir.lib.uwo.ca/etd/4816. Accessed June 15, 2018.

5. Whitelaw WA. Shape and size of the human diaphragm in vivo.

6. Sieck GC, Gransee HM. Respiratory Muscles: Structure, Function, and Regulation. *Colloq Ser Integr Syst Physiol From Mol to Funct*. 2012;4(3):1-96. doi:10.4199/C00057ED1V01Y2012ISP034

7. Pato MPM, Santos NJG, Areias P, et al. Finite element studies of the mechanical behaviour of the diaphragm in normal and pathological cases. 2010. doi:10.1080/10255842.2010.483683

8. Ahn B, Beaver T, Martin T, et al. Phrenic nerve stimulation increases human diaphragm fiber force after cardiothoracic surgery. *Am J Respir Crit Care Med*. 2014;190(7):837-839. doi:10.1164/rccm.201405-0993LE

9. Mills GH, Kyroussis D, Hamnegard CH, Wragg S, Moxham J, Green M. Unilateral magnetic stimulation of the phrenic nerve. *Thorax*. 1995;50(11):1162-1172. http://www.ncbi.nlm.nih.gov/pubmed/8553272. Accessed June 15, 2018.

10. Arora NS, Rochester DF. Effect of body weight and muscularity on human diaphragm muscle mass, thickness, and area. *J Appl Physiol*. 1982;52(1):64-70. http://www.ncbi.nlm.nih.gov/pubmed/7061279. Accessed August 2, 2017.

11. Levine S, Kaiser L, Leferovich J, Tikunov B. Cellular Adaptations in the Diaphragm in Chronic Obstructive Pulmonary Disease. *N Engl J Med*. 1997;337(25):1799-1806. doi:10.1056/NEJM199712183372503

12. Orozco-Levi M, Gea J, Lloreta J, et al. Subcellular adaptation of the human diaphragm in chronic obstructive pulmonary disease. http://erj.ersjournals.com/content/erj/13/2/371.full.pdf. Accessed May 19, 2017.

13. Arora NS, Rochester DF. Effect of body weight and muscularity on human diaphragm muscle mass, thickness, and area.

14. Mathur S, Brooks D, Carvalho CRF. Structural alterations of skeletal muscle in copd. *Front Physiol*. 2014;5:104. doi:10.3389/fphys.2014.00104

15. Orozco-Levi M, Gea J, Lloreta JL, et al. Subcellular adaptation of the human diaphragm in chronic obstructive pulmonary disease. *Eur Respir J*. 1999;13(2):371-378. http://www.ncbi.nlm.nih.gov/pubmed/10065684. Accessed August 2, 2017.

16. Gault ML, Willems MET. Aging, functional capacity and eccentric exercise training. *Aging Dis*. 2013;4(6):351-363. doi:10.14336/AD.2013.0400351

17. Gillies AR, Lieber RL. Structure and function of the skeletal muscle extracellular matrix. *Muscle Nerve*. 2011;44(3):318-331. doi:10.1002/mus.22094

18. Röhrle O, Davidson JB, Pullan AJ. A physiologically based, multi-scale model of skeletal muscle structure and function. *Front Physiol*. 2012;3:358.

doi:10.3389/fphys.2012.00358

19. Srikuea R, Symons TB, Long DE, et al. Association of fibromyalgia with altered skeletal muscle characteristics which may contribute to postexertional fatigue in postmenopausal women. *Arthritis Rheum*. 2013;65(2):519-528. doi:10.1002/art.37763

20. Gronemann ST, Ribel-Madsen S, Bartels EM, Danneskiold-Samsøe B, Bliddal H. Collagen and muscle pathology in fibromyalgia patients. *Rheumatology*. 2004;43(1):27-31. doi:10.1093/rheumatology/keg452

21. Lieber RL, Steinman S, Barash IA, Chambers H. Structural and functional changes in spastic skeletal muscle. *Muscle Nerve*. 2004;29(5):615-627. doi:10.1002/mus.20059

22. Quint LE. Thoracic complications and emergencies in oncologic patients. *Cancer Imaging*. 2009;9 Spec No A(Special issue A):S75-82. doi:10.1102/1470-7330.2009.9031

23. Elefteriades J, Singh M, Tang P, et al. Unilateral diaphragm paralysis: etiology, impact, and natural history. *J Cardiovasc Surg (Torino)*. 2008;49(2):289-295. http://www.ncbi.nlm.nih.gov/pubmed/18431352. Accessed June 15, 2018.

24. Winegrad S. Cardiac myosin binding protein C. *Circ Res*. 1999. doi:10.1161/01.RES.84.10.1117

25. Zaeimdar S. Mechanical Characterization of Breast Tissue Constituents for Cancer Assessment. 2014. https://oatd.org/oatd/record?record=oai%5C%3Asummit.sfu.ca%5C%3A13908. Accessed June 15, 2018.

26. Safshekan F, Tafazzoli-Shadpour M, Abdouss M, Shadmehr MB. Mechanical Characterization and Constitutive Modeling of Human Trachea: Age and Gender Dependency. 2016. doi:10.3390/ma9060456

27. McMahon TA. Muscles, reflexes, and locomotion BT - Reflexes and Motor Control. In: *Reflexes and Motor Control*. ; 1984. doi:10.1016/0021-9290(85)90018-1

28. Odegard GM, Donahue TLH, Morrow DA, Kaufman KR. Constitutive modeling of skeletal muscle tissue with an explicit strain-energy function. *J Biomech Eng*. 2008;130(6):061017. doi:10.1115/1.3002766

29. Teran J, Blemker S, Hing VNT, Fedkiw R. Finite Volume Methods for the Simulation of Skeletal Muscle. *Eurographics/SIGGRAPH Symp Comput Animat*. 2003. doi:10.1561/0600000036

30. Karami E, Gaede S, Lee T-Y, Samani A. Fully automatic algorithm for segmenting full human diaphragm in non-contrast CT Images. In: Gimi B, Molthen RC, eds. ; 2015:941709. doi:10.1117/12.2082634

31. Wheatley BB, Odegard GM, Kaufman KR, Donahue TLH. How does tissue preparation affect skeletal muscle transverse isotropy? *J Biomech*. 2016;49(13):3056-3060. doi:10.1016/j.jbiomech.2016.06.034

32. Zhang G, Chen X, Ohgi J, et al. Biomechanical simulation of thorax deformation using finite element approach. *Biomed Eng Online*. 2016. doi:10.1186/s12938-016-0132-y

33. Farkas GA. Mechanical properties of respiratory muscles in primates. *Respir Physiol*. 1991. doi:10.1016/0034-5687(91)90038-K

34. Remmers JE. Inhibition of inspiratory activity by intercostal muscle afferents. *Respir Physiol*. 1970. doi:10.1016/0034-5687(70)90055-1

35. Lieber RL, Runesson E, Einarsson F, Fridén J. Inferior mechanical properties of spastic muscle bundles due to hypertrophic but compromised extracellular matrix material. *Muscle Nerve*. 2003;28(4):464-471. doi:10.1002/mus.10446

36. Ogneva I V, Lebedev D V, Shenkman BS. Transversal stiffness and Young's

modulus of single fibers from rat soleus muscle probed by atomic force microscopy. *Biophys J*. 2010;98(3):418-424. doi:10.1016/j.bpj.2009.10.028

37.   Haddad SMH, Samani A. A computational model of the left ventricle biomechanics using a composite material approach. *Int J Eng Sci*. 2017;111:61-73. doi:10.1016/j.ijengsci.2016.11.008

38.   Driessen NJB, Bouten CVC, Baaijens FPT. A structural constitutive model for collagenous cardiovascular tissues incorporating the angular fiber distribution. *J Biomech Eng*. 2005;127(3):494-503. http://www.ncbi.nlm.nih.gov/pubmed/16060356. Accessed May 29, 2017.

39.   Alkhouli N, Mansfield J, Green E, et al. The mechanical properties of human adipose tissues and their relationships to the structure and composition of the extracellular matrix. http://ajpendo.physiology.org/content/ajpendo/305/12/E1427.full.pdf. Accessed August 2, 2017.

40.   Fung YC, Skalak R. Biomechanics: Mechanical Properties of Living Tissues. *J Biomech Eng*. 1981. doi:10.1115/1.3138285

41.   Jenkyn TR, Koopman B, Huijing P, Lieber RL, Kaufman KR. Finite element model of intramuscular pressure during isometric contraction of skeletal muscle. *Phys Med Biol*. 2002;47:4043-4061. https://pdfs.semanticscholar.org/9b34/a28b07c890e9c0628809dc785139a8a8973c.pdf?_ga=2.266393421.213360555.1521198737-124438306.1521198737. Accessed March 16, 2018.

42.   Linden BJJJ van der. Mechanical modeling of skeletal muscle functioning. May 1998. https://research.utwente.nl/en/publications/mechanical-modeling-of-skeletal-muscle-functioning. Accessed March 16, 2018.

43.   Morrow DA, Haut Donahue TL, Odegard GM, Kaufman KR. Transversely isotropic tensile material properties of skeletal muscle tissue. *J Mech Behav*

Biomed Mater. 2010;3(1):124-129. doi:10.1016/j.jmbbm.2009.03.004

44.   Martins JAC, Pato MPM, Pires EB. A finite element model of skeletal muscles. *Virtual Phys Prototyp*. 2006. doi:10.1080/17452750601040626

45.   Van Naarden Braun K, Doernberg N, Schieve L, Christensen D, Goodman A, Yeargin-Allsopp M. Birth Prevalence of Cerebral Palsy: A Population-Based Study. *Pediatrics*. 2016;137(1):1. doi:10.1542/peds.2015-2872

46.   Rizzo MA, Hadjimichael OC, Preiningerova J, Vollmer TL. Prevalence and treatment of spasticity reported by multiple sclerosis patients. *Mult Scler J*. 2004;10(5):589-595. doi:10.1191/1352458504ms1085oa

47.   Lieber RL, Runesson E, Einarsson F, Fridén J. Inferior mechanical properties of spastic muscle bundles due to hypertrophic but compromised extracellular matrix material. *Muscle Nerve*. 2003;28(4):464-471. doi:10.1002/mus.10446

48.   Stylianopoulos T, Barocas VH. Volume-averaging theory for the study of the mechanics of collagen networks. *Comput Methods Appl Mech Eng*. 2007;196(31):2981-2990. doi:10.1016/j.cma.2006.06.019

49.   Myers KM, Hendon CP, Gan Y, et al. A continuous fiber distribution material model for human cervical tissue. *J Biomech*. 2015;48(9):1533-1540. doi:10.1016/j.jbiomech.2015.02.060

50.   Barocas VH, Tranquillo RT. An anisotropic biphasic theory of tissue-equivalent mechanics: the interplay among cell traction, fibrillar network deformation, fibril alignment, and cell contact guidance. *J Biomech Eng*. 1997;119(2):137-145. http://www.ncbi.nlm.nih.gov/pubmed/9168388. Accessed October 3, 2017.

51.   Mow VC, Kuei SC, Lai WM, Armstrong CG. Biphasic Creep and Stress Relaxation of Articular Cartilage in Compression: Theory and Experiments. *J Biomech Eng*. 1980;102(1):73. doi:10.1115/1.3138202

52.   Hill MR, Simon MA, Valdez-Jasso D, Zhang W, Champion HC, Sacks MS.

Structural and Mechanical Adaptations of Right Ventricle Free Wall Myocardium to Pressure Overload. *Ann Biomed Eng*. 2014;42(12):2451-2465. doi:10.1007/s10439-014-1096-3

53. Bell RD, MacDougall JD, Billeter R, Howald H. Muscle fiber types and morphometric analysis of skeletal msucle in six-year-old children. *Med Sci Sports Exerc*. 1980;12(1):28-31. http://www.ncbi.nlm.nih.gov/pubmed/7392899. Accessed May 19, 2017.

54. Yoshikawa Y, Yasuike T, Yagi A, Yamada T. Transverse Elasticity of Myofibrils of Rabbit Skeletal Muscle Studied by Atomic Force Microscopy. *Biochem Biophys Res Commun*. 1999;256(1):13-19. doi:10.1006/bbrc.1999.0279

55. Ogneva I V, Lebedev D V, Shenkman BS. Transversal stiffness and Young's modulus of single fibers from rat soleus muscle probed by atomic force microscopy. *Biophys J*. 2010;98(3):418-424. doi:10.1016/j.bpj.2009.10.028

56. Nie X, Cheng J-I, Chen WW, Weerasooriya T. Dynamic Tensile Response of Porcine Muscle. *J Appl Mech*. 2011;78(2):021009. doi:10.1115/1.4002580

57. Takaza M, Moerman KM, Gindre J, Lyons G, Simms CK. The anisotropic mechanical behaviour of passive skeletal muscle tissue subjected to large tensile strain. *J Mech Behav Biomed Mater*. 2013;17:209-220. doi:10.1016/j.jmbbm.2012.09.001

58. Sokolis DP. Passive mechanical properties and constitutive modeling of blood vessels in relation to microstructure. *Med Biol Eng Comput*. 2008;46(12):1187-1199. doi:10.1007/s11517-008-0362-7

59. Dagan D, Be'ery M, Gefen A. Single-trabecula building block for large-scale finite element models of cancellous bone. *Med Biol Eng Comput*. 2004;42(4):549-556. http://www.ncbi.nlm.nih.gov/pubmed/15320466. Accessed May 29, 2017.

60. Haddad SMH, Samani A. A novel micro-to-macro approach for cardiac tissue mechanics. *Comput Methods Biomech Biomed Engin*. 2017;20(2):215-229.

doi:10.1080/10255842.2016.1214270

61. Ogneva I V, Lebedev D V, Isaev-Ivanov V V, Shenkman BS. [Spatial distribution of transverse stiffness of relaxed and activated rat soleus myofibers]. *Biofizika*. 53(6):1073-1077. http://www.ncbi.nlm.nih.gov/pubmed/19137695. Accessed October 4, 2017.

62. Transverse Elasticity of Myofibrils of Rabbit Skeletal Muscle Studied by Atomic Force Microscopy. *Biochem Biophys Res Commun*. 1999;256(1):13-19. doi:10.1006/BBRC.1999.0279

63. Hoppeler H, Luthi P, Claassen H, Weibel ER, Howald H. The ultrastructure of the normal human skeletal muscle. *Pflugers Arch Eur J Physiol*. 1973;344(3):217-232. doi:10.1007/BF00588462

64. Power GA, Dalton BH, Rice CL. Human neuromuscular structure and function in old age: A brief review. *J Sport Heal Sci*. 2013;2(4):215-226. doi:10.1016/j.jshs.2013.07.001

65. Rice CL, Cunningham DA, Paterson DH, Lefcoe MS. Arm and leg composition determined by computed tomography in young and elderly men. *Clin Physiol*. 1989;9(3):207-220. http://www.ncbi.nlm.nih.gov/pubmed/2743739. Accessed July 11, 2017.

66. Overend TJ, Cunningham DA, Paterson DH, Lefcoe MS. Thigh composition in young and elderly men determined by computed tomography. *Clin Physiol*. 1992;12(6):629-640. http://www.ncbi.nlm.nih.gov/pubmed/1424481. Accessed July 11, 2017.

67. Luther PK, Padrón R, Ritter S, Craig R, Squire JM. Heterogeneity of Z-band Structure Within a Single Muscle Sarcomere: Implications for Sarcomere Assembly. *J Mol Biol*. 2003;332(1):161-169. doi:10.1016/S0022-2836(03)00883-0

68. Burgoyne T, Morris EP, Luther PK. Three-Dimensional Structure of Vertebrate

Muscle Z-Band: The Small-Square Lattice Z-Band in Rat Cardiac Muscle. *J Mol Biol*. 2015;427(22):3527-3537. doi:10.1016/j.jmb.2015.08.018

69.   Polla B, D 'antona G, Bottinelli R, Reggiani C. Respiratory muscle fibres: specialisation and plasticity. *Thorax*. 2004;59:808-817. doi:10.1136/thx.2003.009894

70.   Karjalainen J, Tikkanen H, Hernelahti M, Kujala UM. Muscle fiber-type distribution predicts weight gain and unfavorable left ventricular geometry: a 19 year follow-up study. *BMC Cardiovasc Disord*. 2006;6:2. doi:10.1186/1471-2261-6-2

71.   Kiessling K-H, Pilstrum L, Karlsson " A N J, Piehl IN. MITOCHONDRIAL VOLUME I N SKELETAL MUSCLE FROM Y O U N G A N D OLD PHYSICALLY U N T R A I N E D A N D T R A I N E D HEALTHY M E N A N D FROM ALCOHOLICS. *Clin Sci*. 1973;44:547-554. http://www.clinsci.org/content/ppclinsci/44/6/547.full.pdf. Accessed May 19, 2017.

72.   Tam CS, Covington JD, Bajpeyi S, et al. Weight gain reveals dramatic increases in skeletal muscle extracellular matrix remodeling. *J Clin Endocrinol Metab*. 2014;99(5):1749-1757. doi:10.1210/jc.2013-4381

73.   Physiological Society (Great Britain). Meeting. T, Isaka T, Fujita S, Hamaoka T. *Proceedings of the Physiological Society*. Physiological Society; 2006. http://www.physoc.org/proceedings/abstract/Proc Physiol Soc 26PC79. Accessed May 28, 2017.

74.   Zhu R, Wen C, Li J, Harris MB, Liu Y-Y, Kuo C-H. Lipid storage changes in human skeletal muscle during detraining. *Front Physiol*. 2015;6:309. doi:10.3389/fphys.2015.00309

75.   Roeder BA, Kokini K, Sturgis JE, Robinson JP, Voytik-Harbin SL. Tensile mechanical properties of three-dimensional type I collagen extracellular matrices

with varied microstructure. *J Biomech Eng*. 2002;124(2):214-222.
http://www.ncbi.nlm.nih.gov/pubmed/12002131. Accessed May 28, 2017.

76. Seyfi B, Sabzalinejad M, Haddad SMH, Fatouraee N, Samani A. A FSI-based
     structural approach for micromechanical characterization of adipose tissue. In:
     Krol A, Gimi B, eds. International Society for Optics and Photonics;
     2017:101370G. doi:10.1117/12.2254652

77. Meyer GA, Lieber RL. Elucidation of extracellular matrix mechanics from muscle
     fibers and fiber bundles. *J Biomech*. 2011;44(4):771-773.
     doi:10.1016/j.jbiomech.2010.10.044

78. Deschenes MR. Effects of aging on muscle fibre type and size. *Sports Med*.
     2004;34(12):809-824. http://www.ncbi.nlm.nih.gov/pubmed/15462613. Accessed
     May 28, 2017.

79. Volpi E, Nazemi R, Fujita S. Muscle tissue changes with aging. *Curr Opin Clin
     Nutr Metab Care*. 2004;7(4):405-410.
     http://www.ncbi.nlm.nih.gov/pubmed/15192443. Accessed May 28, 2017.

80. Marcus RL, Addison O, Kidde JP, Dibble LE, Lastayo PC. Skeletal muscle fat
     infiltration: impact of age, inactivity, and exercise. *J Nutr Health Aging*.
     2010;14(5):362-366. http://www.ncbi.nlm.nih.gov/pubmed/20424803. Accessed
     May 28, 2017.

81. Menshikova E V, Ritov VB, Fairfull L, Ferrell RE, Kelley DE, Goodpaster BH.
     Effects of exercise on mitochondrial content and function in aging human skeletal
     muscle. *J Gerontol A Biol Sci Med Sci*. 2006;61(6):534-540.
     http://www.ncbi.nlm.nih.gov/pubmed/16799133. Accessed May 29, 2017.

82. Berria R, Wang L, Richardson DK, et al. Increased collagen content in insulin-
     resistant skeletal muscle. *AJP Endocrinol Metab*. 2005;290(3):E560-E565.
     doi:10.1152/ajpendo.00202.2005

83. Jenkyn TR, Koopman B, Huijing P, Lieber RL, Kaufman KR. Finite element

model of intramuscular pressure during isometric contraction of skeletal muscle. *Phys Med Biol*. 2002;47(22):4043-4061. doi:10.1088/0031-9155/47/22/309

84. Takaza M, Moerman KM, Gindre J, Lyons G, Simms CK. The anisotropic mechanical behaviour of passive skeletal muscle tissue subjected to large tensile strain. *J Mech Behav Biomed Mater*. 2013;17:209-220. doi:10.1016/j.jmbbm.2012.09.001

85. Jannapureddy SR, Patel ND, Hwang W, Boriek AM. Selected Contribution: Merosin deficiency leads to alterations in passive and active skeletal muscle mechanics. *J Appl Physiol*. 2003;94(6). http://jap.physiology.org/content/94/6/2524. Accessed October 4, 2017.

86. Coelho B, Karami E, Haddad SMH, Seify B, Samani A. A biomechanical approach for *in vivo* diaphragm muscle motion prediction during normal respiration. In: Webster RJ, Fei B, eds. International Society for Optics and Photonics; 2017:1013505. doi:10.1117/12.2254590

87. Fuerst B, Mansi T, Carnis F, et al. Patient-specific biomechanical model for the prediction of lung motion from 4-D CT images. *IEEE Trans Med Imaging*. 2015. doi:10.1109/TMI.2014.2363611

88. Seyfi B, Santhanam AP, Ilegbusi OJ. A Biomechanical Model of Human Lung Deformation Utilizing Patient-Specific Elastic Property. *J Cancer Ther*. 2016. doi:10.4236/jct.2016.76043

89. Cervĩo LI, Chao AKY, Sandhu A, Jiang SB. The diaphragm as an anatomic surrogate for lung tumor motion. *Phys Med Biol*. 2009. doi:10.1088/0031-9155/54/11/017

90. Cerviño LI, Chao AKY, Sandhu A, Jiang SB. The diaphragm as an anatomic surrogate for lung tumor motion. *Phys Med Biol*. 2009;54(11):3529-3541. doi:10.1088/0031-9155/54/11/017

91. Promayon E, Baconnier P. A 3D discrete model of the diaphragm and human

trunk. August 2008. http://arxiv.org/abs/0808.0339. Accessed January 13, 2017.

92.   Ladjal H, Saade J, Beuve M, Azencot J, Moreau J-M, Shariat B. 3D
      Biomechanical Modeling of the Human Diaphragm Based on CT Scan Images. In:
      Springer, Berlin, Heidelberg; 2013:2188-2191. doi:10.1007/978-3-642-29305-
      4_574

93.   Pato MPM, Santos NJG, Areias P, et al. Finite element studies of the mechanical
      behaviour of the diaphragm in normal and pathological cases. *Comput Methods
      Biomech Biomed Engin*. 2011;14(6):505-513. doi:10.1080/10255842.2010.483683

94.   Santos NJG. Preliminary Biomechanical Studies on the Diaphragmatic Function in
      Control and Patients with Loss of Motor Units. 2009.
      https://fenix.tecnico.ulisboa.pt/downloadFile/395139480394/resumo.pdf. Accessed
      August 2, 2017.

95.   Troyer A De, Wilson TA. Action of the diaphragm on the rib cage. *J Appl Physiol*.
      2016. doi:10.1152/japplphysiol.00268.2016

96.   Pandy MG, Zajac FE, Sim E, Levine WS. An optimal control model for
      maximum-height human jumping. *J Biomech*. 1990. doi:10.1016/0021-
      9290(90)90376-E

97.   Karami E, Wang Y, Gaede S, Lee T-Y, Samani A. Anatomy-based algorithm for
      automatic segmentation of human diaphragm in noncontrast computed tomography
      images. *J Med Imaging*. 2016. doi:10.1117/1.JMI.3.4.046004

98.   Sieck GC, Gransee HM. Respiratory Muscles: Structure, Function, and Regulation.
      Colloq Ser Integr Syst Physiol From Mol to Funct. 2012;4(3):1-96.
      doi:10.4199/C00057ED1V01Y2012ISP034

99.   Ladjal H, Shariat B, Azencot J, Beuve M. Appropriate biomechanics and
      kinematics modeling of the respiratory system: Human diaphragm and thorax. In:
      2013 IEEE/RSJ International Conference on Intelligent Robots and Systems.
      IEEE; 2013:2004-2009. doi:10.1109/IROS.2013.6696623

100. Saadé J, Didier A-L, Buttin R, et al. A PRELIMINARY STUDY FOR A BIOMECHANICAL MODEL OF THE RESPIRATORY SYSTEM.

101. Sieck GC, Ferreira LF, Reid MB, Mantilla CB. Mechanical properties of respiratory muscles. *Compr Physiol*. 2013. doi:10.1002/cphy.c130003

102. Polla B, D'Antona G, Bottinelli R, Reggiani C. Respiratory muscle fibres: specialisation and plasticity. *Thorax*. 2004;59(9):808-817. doi:10.1136/thx.2003.009894

103. CORDA M, VONEULER C, LENNERSTRAND G. PROPRIOCEPTIVE INNERVATION OF THE DIAPHRAGM. *J Physiol*. 1965;178(1):161-177. http://www.ncbi.nlm.nih.gov/pubmed/14298107. Accessed January 12, 2018.

104. Lieber RL, Runesson E, Einarsson F, Fridén J. Inferior mechanical properties of spastic muscle bundles due to hypertrophic but compromised extracellular matrix material. *Muscle Nerve*. 2003;28(4):464-471. doi:10.1002/mus.10446

105. Rospars JP, Meyer-Vernet N. Force per cross-sectional area from molecules to muscles: A general property of biological motors. *R Soc Open Sci*. 2016. doi:10.1098/rsos.160313

106. Choi M, Lee N, Kim A, et al. Evaluation of diaphragmatic motion in normal and diaphragmatic paralyzed dogs using m-mode ultrasonography. *Vet Radiol Ultrasound*. 2014. doi:10.1111/vru.12126

107. Elefteriades J, Singh M, Tang P, et al. Unilateral diaphragm paralysis: Etiology, impact, and natural history. *J Cardiovasc Surg (Torino)*. 2008.

108. D. N, D. M, D. Y, N. D. Unilateral diaphragmatic paralysis: How far to investigate? *Respirology*. 2012.

109. Pickering M, Jones JFX. The diaphragm: Two physiological muscles in one. *J Anat*. 2002. doi:10.1046/j.1469-7580.2002.00095.x

110. Rospars J-P, Meyer-Vernet N. Force per cross-sectional area from molecules to muscles: a general property of biological motors. *R Soc open Sci*. 2016;3(7):160313. doi:10.1098/rsos.160313

Chapter 2

2 « A micro to macro mechanical approach for skeletal muscle tissue mechanical characterization »

2.1 « Introduction »

The Passive mechanical properties of skeletal muscles have been studied under tension and compression for many reasons. Accurate measurement of these properties is important in many applications such as development of computational models that capture their physiology. These properties are essential in developing models to simulate muscular deformation resulting from contraction or external loading[18]. They are also necessary for development of biomaterials to substitute muscle tissue. Changes in the mechanical response of both passive and active components of muscle tissue can occur as a result of various pathologies which lead to altered mechanical properties of the tissue[14]. According to the American Association of Neurological Surgeons, muscle spasticity affects more than 12 million people worldwide and affects as much as 77.4% and 84% of people with cerebral palsy and multiple sclerosis, respectively[45,46]. Spasticity negatively affects muscles and has been shown to compromise the passive mechanics of muscle tissue through alteration of its ultrastructure[47]. Fibromyalgia is another pertinent disease which is associated with reduction in muscle collagen making it more susceptible to micro injury[46]. Skeletal muscle tissue is complex, however, a structural approach that assumes the mechanical behaviour of tissue is a result of superposition of the mechanical responses of its internal micro-constituents, can be employed to model its intrinsic properties. Through FE implementation, this approach incorporates tissue constituent volume and orientation along with their specific mechanical properties in the model[48]. This approach is capable of simulating various normal and pathological tissue scenarios to provide ranges of their property parameters. Various structural approaches have been used over recent years to provide realistic models for tissues and materials[49,37,38]. Structural approaches pose an advantage over phenomenological modelling which relies on a strain energy function to describe the general behavior but has strict reliance on experimental testing to determine a

specific tissue's parameters. Parameters obtained for muscle tissue using phenomenological modelling are valid for the specific tested tissue specimen, hence cannot represent the behaviour of all muscle tissue types and variations effectively. While mechanical testing of *ex vivo* muscle tissue is possible for broad tissue mechanical characterization, it may not be technically feasible due to the need for a large number of various fresh tissue samples in addition to challenges of rigor-mortis. The continuum modelling approach is another alternative that considers all tissue constituents and their interaction to derive a comprehensive constitutive model. The continuum approach deals with holistic physical properties and represents their properties as a tensor[50,51]. While it can be highly accurate this approach is inherently complex. AS such, given the readily available information regarding the physical orientation of skeletal muscle tissue's microstructure and composition, the structural approach has been used in this study.

Among types of muscle tissue, the mechanics of cardiac tissue has been studied[38,52]. Most models use a composite approach with myofibril and lumped non-myofibril components. While lacking flexibility to represent intrinsic properties of wide spectrum of a tissue type, such models can yield unrealistic predictions with respect to tissue composition due to over simplification. Fortunately, it is possible to digest and isolate specific microstructural components of skeletal muscle tissue and perform mechanical testing[47,53,54,55]. With such information, our model can be developed to include a multitude of the major skeletal muscle tissue constituents. If a constituent's volume, mechanical properties, and approximate distribution in the tissue is known, it can be incorporated into the proposed model. Such adaptability is advantageous due to the various alterations of tissue microstructure associated with different pathologies.

Passive tensile stress-strain experimental data has been acquired by many groups across a range of animals[56,43,28,57,31]. Discrepancies among past investigations exist in relation to the longitudinal and cross fiber stiffness which characterize the transverse isotropy of the tissue. These discrepancies have been majorly attributed to differences in tissue sample preparations[31], although anatomical disparities due to species variation are also present. Recent work by Wheatley et al. on rabbits aimed at determining the effects of skeletal muscle tissue sample preparation agreed with the results of several investigators that found

that the transverse fiber direction is the stiffest[20]. This is true when experimentation is done on fresh, hydrated, and never frozen samples; which is most indicative of *in-vivo* mechanics. We begin our novel approach for skeletal muscle tissue modeling geared towards capturing the mechanics of *in-vivo* skeletal muscle tissue, to achieve reasonably accurate realism and account for observations in a clinical setting. Using the major constituents, the preliminary model (absent Z-disc incorporation) behaved similarly to the longitudinal experimental results presented by Takaza et al. for porcine[57]. Z-discs were then incorporated to account for transverse isotropy.

Our model follows a micro to macro mechanical approach to determine skeletal muscle tissue properties pertaining to its intrinsic hyperelasticity and anisotropy. It is capable of capturing mechanical changes realistically because the overall mechanical properties of a tissue is known to be a function of its microstructural constituents and their associated volume and distribution[58,59,60]. The novel incorporation of Z-disc elements in the proposed model serves the purpose of more accurately capturing the transverse isotropy of the tissue. Atomic force microscopy has shown that the transverse stiffness of myofibrils is greatest at the projection of the Z-discs[61]. Attempts have been made towards characterizing Z-disc mechanical properties using atomic force microscopy, however, the microscopic nature of the technique involves elastic contributions from other structures and the potential for actomyosin thin and thick filament slippage. This slippage is likely to result in underestimation of the Z-disc lattice stiffness[36,62]. The computational model proposed in this work is developed for characterising the passive tensile mechanical properties of skeletal muscle while estimating the mechanical properties of the Z-discs through model optimization. This estimation may be more realistic than estimations obtained through atomic force microscopy as it does not involve the experimentally inevitable errors due to other microstructures and muscle filament slippage. The developed model considers hyperelasticity while its anisotropy is self-contained. The tissue model's sensitivity to constituents is assessed through sensitivity analysis. A case study is performed to assess the effects of altering the tissue's muscle fiber volume percentage or compromised muscle fiber mechanics due to a pathological condition. The results have been shown to capture the transversely isotropic behaviour of skeletal muscle reasonably accurately.

2.2   « Materials and Methods »

The micro to macro structural approach proposed to characterize skeletal muscle in this study requires data pertaining to its complex and variable microstructure. Tissue morphometric techniques utilizing electron or light microscopy reveal the volumetric quantities of different active and passive components of the tissue. Studies performed on pathological tissues provide information regarding alterations in the microstructure because of a shift in the volume percentages of their constituents.

In this work, we assume that the macroscopic mechanical behaviour of whole muscle tissue results from the mechanics of the predominant constituents. The major mechanical components in skeletal muscle include the skeletal myocytes and their surrounding extracellular matrix (ECM). Myocytes include various structures such as myofibrils, mitochondria, Z-discs, and sarcolemma. Myofibers are both passive and active because they generate muscle contraction forces. Morphometric studies of skeletal muscle reveal that muscle fibers occupy approximately 83% of their volume[53,47,63]. It has also been found that depending on the muscle group, the amount of non-contractile tissue in old and young individuals are respectively 8-18% and 2-5% of the whole muscle cross-sectional area[64,65,66]. The sarcolemma is a tubular sheath that envelops the fibers and plays an important role in the structural integrity of the fibers and their passive mechanics[17]. For this reason, myofibril bundles were considered as the major constituent in our model. Recent studies using atomic force microscopy have shown that the transverse stiffness of myofibrils changes along the length of fibers with a distinctly stiffer region corresponding to the Z-band[55,54]. The Z-band widths vary depending on fiber type; fast twitch fibers have narrower bands (~30-50 nm) whereas slow twitch fibers have wide Z-bands (~100-140 nm)[55]. Visualizing Z-band width is a common method for fiber type differentiation. Z-bands are multilayered lattice structures with a net orientation transverse to muscle fibers, easily observed in electron micrographs[67,68]. Z-bands have been associated with increased lateral stiffness along muscle fibers, reaching a maximum at the projections of the Z-discs[55]. In this work, skeletal muscle was considered for the model which has approximately 60% slow and 40% fast twitch fiber types resulting in a ~6% Z-band volume using a rest sarcomere length of 2 µm[69,11,47,70]. Z-discs were therefore considered important

in characterizing the muscle lateral stiffness in the model, hence were incorporated into myofibril regions.   Figure 2-1 shows a schematic illustrating how Z-discs were incorporated into the FE model.

(a)   (b)   (c)
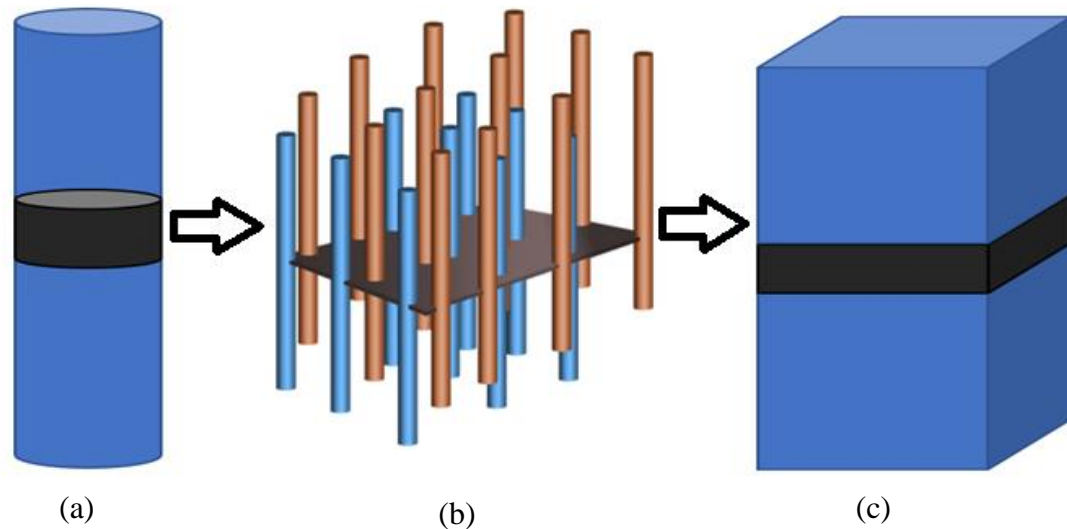
Figure 2-1 (a) The concept of a Z-disc region (black disc) between anti-parallel bundle of sarcomeres, (b) the Z-disc region as a black plane traversing actin filaments originating from adjacent sarcomeres coloured light brown and blue, (c) the Z-discs were modelled using a FE scheme in the proposed model where the blue and black regions represent distinct finite elements.

The ECM is another important part of skeletal muscle tissue. It has various constituents and occupies the volume outside of myocytes. Mitochondria is an abundant structure in muscle tissue because of the high-energy demands of muscle compared to other organs of the body. The volume percentage of extramyocellular mitochondria in the ECM of skeletal muscle is approximately 7% and can vary by several percent depending on the specific muscle and subject[12,71].   As such, mitochondria were selected as one of the major constituents of the ECM. Collagen is another essential constituent of the ECM with a relatively high stiffness under increasing tension. It's volume in skeletal muscle ECM is estimated at 1-10%[17]. The presence of extramyocellular fat is a third important component of the ECM which can range from as low as 1.5% and up to 11% volume in elderly, obese individuals[72,73,74].   Table 2-1 shows typical volume percentage of each constituent

predicted for normal skeletal diaphragm muscle tissue according to the given ranges. However, constituent volume percentages are known to vary from across muscles and individuals as revealed using morphometric studies.

Table 2-1 Major Constituents of normal diaphragm muscle tissue and their volume percentage.

Constituent	Myofibrils (including Z-disc)	Mitochondria	Collagen	Fat
Volume percentage	~83	~7	~3	~7

2.2.1   Muscle Tissue Modelling and Z-disc Hyperelastic Parameter Estimation

As indicated earlier, skeletal muscle tissue is a composite material which mainly includes myofibril and ECM components. This is consistent with the renowned Hill's model which contains both active and passive elements; this work focuses on the passive extensional behaviour of skeletal muscle tissue. The presence of the myofibril components and their alignment in conjunction with the transverse Z-disc structures, leads to a self-contained anisotropy. Bonding between the myofibril and ECM results in load sharing between each component which maintains mechanical equilibrium under tension. The muscle tissue is resolved into two main parts: ECM and myofibrils where the Z-discs are contained in the latter. Figure 2-2 illustrates the steps that will be taken toward development of the whole muscle tissue model. According to this figure, our proposed model involves two steps. In the first step, the ECM component is modelled using FEM where pertinent ultrastructural constituents with known intrinsic properties are incorporated and assembled before a uniaxial test is simulated to obtain a simulated stress-strain response. In the second step, the whole tissue is simulated whereby the ECM represented by the stress-strain response obtained from the first step is combined with myofibrils, including Z-discs, again through FE modeling. Details of the two steps are given in the following sections.
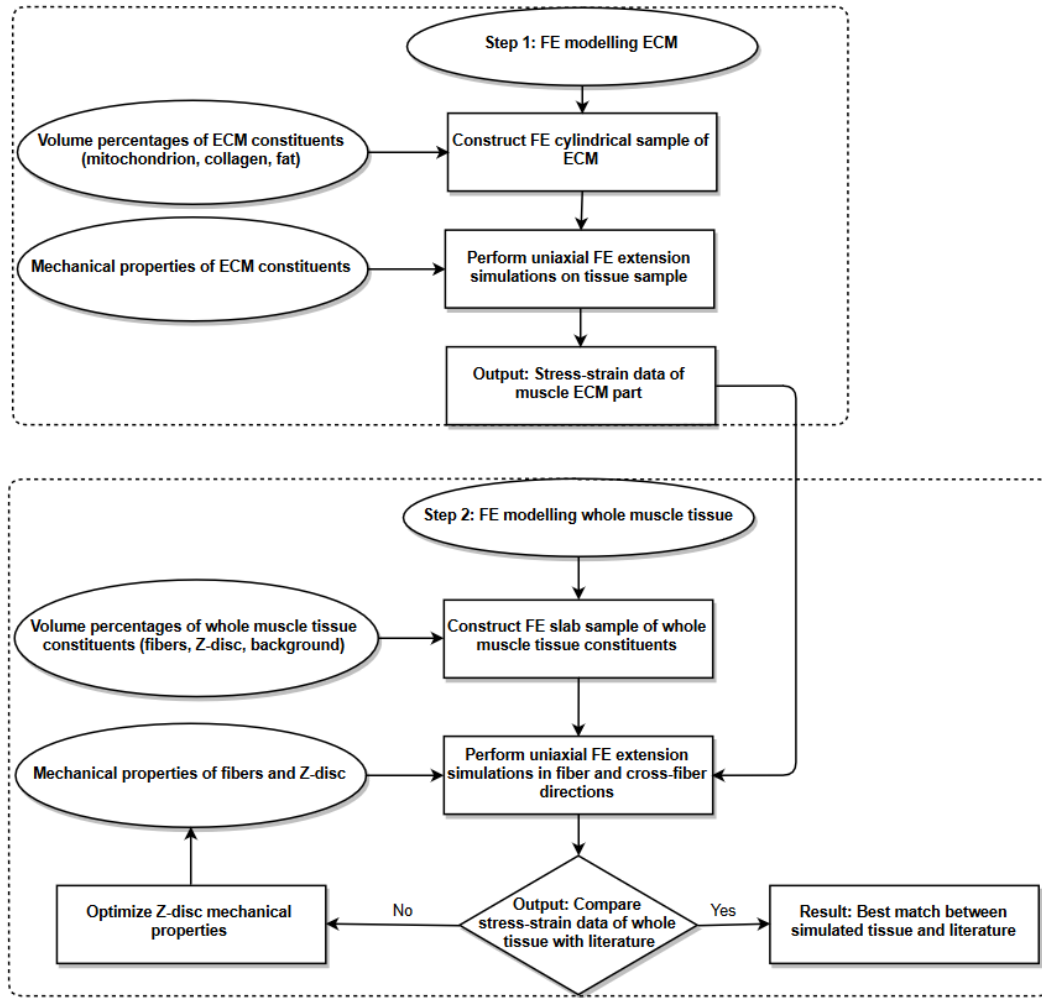
Figure 2-2 Flowchart illustrating the proposed skeletal muscle tissue modelling approach.

2.2.2   Step 1 - ECM Part Modelling

A cylindrical sample was considered for the ECM part's FE model. As aforementioned, the ECM is a structure comprised of mainly mitochondria, collagen, and fat. Considering their volume percentage given in Table 2-1, we assumed uniform distribution of elements corresponding to each of these constituents. Depending on the element type, mechanical properties have been assigned according to the literature. Stress-strain data for mitochondria, collagen, and fat have been reported in the literature[75,60,39,76]. In this work,

these constituents are modelled according to the following Yeoh hyperelastic model for an incompressible material:

$$W = \sum_{i=1}^{n} C_i \left(I_1 - 3\right)^i$$ (1)

where C_i refers to the hyperelastic parameters of the tissue and I_1 represents the first strain invariant of the Cauchy-Green deformation tensors. The Yeoh model is commonly considered to be a good model for incompressible soft tissues[26]. According to the literature, the C_1, C_2, and C_3 parameters for the mitochondrion are 500, 2000, and 0 Pa, respectively[60].

The mechanical properties of collagen and fat were also obtained from stress-strain experimental data[75,39]. The data was fitted to the Ogden and Yeoh hyperelastic models to determine corresponding hyperelastic parameters. These models led to high quality fit of the experimental data. Using the calculated Ogden and Yeoh hyperelastic along with estimated volume percentages of each constituent in the ECM part, a uniaxial FE simulation was performed on a cylindrical sample model of ECM part containing 16500 hexahedral elements as seen in Figure 2-3. Axial strains were varied incrementally from 0 to 35% with prescribed displacement boundary conditions. This led to uniformly distributed axial stresses which were calculated in ABAQUS FE solver (Dassault Systemes SIMULIA Corp, Waltham, MA 02451, USA).

2.2.3   Step 2 - Whole Skeletal Muscle Tissue Modelling

2.2.3.1   Myofibril and Z-disc Composite Model

A schematic of a group of aligned myofibrils along with transversely aligned Z-discs is illustrated in Figure 2-1. To build this composite model, constitutive models are required for the myofibril and Z-disc parts. For the myofibril part, stress-strain data was extracted

from experimental data reported by Lieber et al[47] for normal skeletal muscle. The data was used as input test data for the Yeoh hyperelastic model[47,46].
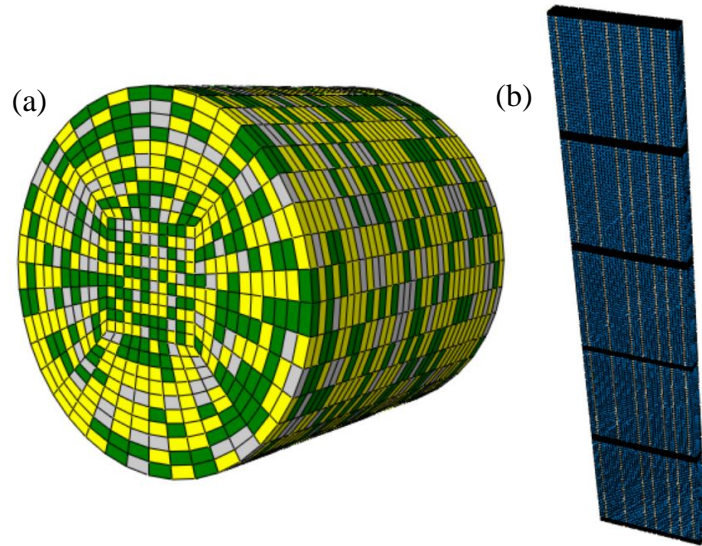
Figure 2-3 FE model of (a) cylindrical sample of ECM part composed of amounts of mitochondrion (green), fat (yellow), and collagen (grey) given in Table 2-1 and (b) slab sample of whole skeletal muscle tissue composed of ECM (white), muscle fiber bundles (blue) and Z-disc elements (black).

As aforementioned, the Z-discs occupy ~6% of the myofibril part and have a structured orientation perpendicular to the muscle fiber direction. In this work, the Z-discs were assumed to follow a Neo-Hookean hyperelastic model which led to a good fit to experimental data. To our knowledge, an estimation of hyperelastic parameter of intact *ex vivo* Z-discs is unavailable. To provide such estimation, the Neo-Hookean hyperelastic parameter of Z-discs was estimated using optimization by iteratively adjusting its value in the whole muscle tissue FE model until simulated stress-strain data in fiber and cross-fiber directions matched corresponding experimental data[57]. It is predicted that the Z-disc stiffness will account for the increased stiffness in the cross-fiber direction as seen in fresh, whole muscle tissue[57,31].

2.2.3.2   Whole Tissue Model

For the whole skeletal muscle tissue, FE simulations of uniaxial extensions in fiber and across-fiber directions were performed on a slab containing 8000 hexahedral elements shown in Figure 2-3. This model includes five muscle and four Z-disc layers. Increasing the number of these layers did not lead to significant change in resulting hyperelastic parameters of skeletal muscle tissue. The second order Yeoh model for both myofibril and ECM constituents along with Neo-Hookean model for the Z-discs yielded the best fit with data available in the literature[47,77]. Uniaxial extension of the slab was simulated using ABAQUS FE solver along and across the muscle fiber directions ranging up to 30% and 15% strain, respectively.   This allowed for a complete comparison with existing experimental data obtained with these maximum strain values limited to avoid significant disintegration of muscle tissue. Stress-strain data of normal skeletal muscle tissue in fiber and cross fiber direction was obtained and compared to recent studies that aim to quantify the passive tensile behaviour of *in vivo* skeletal muscle tissue.

2.2.4   Case Studies

Changes to skeletal muscle can be very complex[78], including alterations to ECM constituents as well as muscle fiber percentage. For example, increasing extracellular muscle fat content, is one of the involuntary processes commonly resulting from aging, immobility, and obesity combined[79,80]. It has also been shown that a lack of exercise can lead to a reduction in mitochondrion content, as the energy demands of the muscle are often minimal[81]. Berria et al. concluded that there is increased collagen content in the ECM of muscle in insulin-resistant skeletal muscle, a phenomenon that can be found among diabetics[82].

The To demonstrate the adaptability of the proposed method to model healthy skeletal muscle tissue the muscle fiber constituent volume percentage was varied to encompass realistic values including low, medium, and high amounts of myofibrils. Furthermore, to model spastic muscles, the mechanics of muscle fiber bundles were altered to be characteristic of spastic muscle.   Spastic muscle fiber bundle stress-strain data was extracted from Lieber et al[47] and fit to the Yeoh hyperelastic model. Tensile mechanical

simulations were performed for changes in muscle fiber percentages and to investigate how spastic muscle affects the overall mechanics of the muscle tissue.

2.2.5   Sensitivity Analysis to ECM Constituent Volumes Alteration

Sensitivity analysis was performed to find sensitivity of skeletal muscle stiffness parameters w.r.t changes in each major constituent. For this purpose, volume percentages of individual ECM constituents were varied by ±1%. The addition and subtraction of 1% of each constituent was analysed at three regimes for passive tensile simulations along and across fiber directions to determine the sensitivity related to each constituent variation. The along-fiber direction regimes selected for analysis were 10, 20, and 30% strain, whereas across fiber direction regimes correspond to 5, 10, and 15% strain corresponding to small, medium and large strain regimes, respectively. This is consistent with the whole tissue extensional analysis for each direction. Comparing the difference in instantaneous moduli as a result of 1% constituent addition to that of 1% subtraction at each strain regime was done to give insight as to how the overall 2% change in constituent volume percentage effects the whole tissue mechanics. FE models were constructed per the altered volume percentages of constituents. The cylindrical model was again used for the ECM part stress-strain data acquisition followed by whole tissue modelling using the new ECM part mechanics.

2.2.6   Hyperelastic Model of Passive Skeletal Muscle

To obtain an anisotropic hyperelastic model for passive skeletal muscle, stress-strain data generated using the proposed computational model are used to fit anisotropic hyerelastic models available in the literature. Researchers including Jenkyn et al. and Linden developed two-dimensional FE models of skeletal muscle based on *in vivo* experimentation on rabbits and rats, respectively[83,42]. Their model's mechanics are based on a variation of the Fung hyperelastic model whose parameters for determining strain energy density are attained experimentally. The parameters attained for the models account for the passive stiffness related to longitudinal and transverse directions in the tissue. The anisotropic strain energy density equations are as follows:

$$W^{\text{parallel}}(e_2) = \frac{k}{a_2}(e^{a_2 e_2} - a_2 e_2)$$

$$(2)$$

$$W^{\text{perpendicular}}(e_1) = \frac{k}{a_1}(e^{a_1 e_1} - a_1 e_1)$$

where a_1 and a_2 are the hyperelastic parameters related to the passive stiffness in cross fiber and fiber directions, respectively. k is another hyperelastic parameter related to the materials initial passive stiffness. e_1 and e_2 are Green strains in cross fiber and fiber directions, respectively. The experimental protocol performed by Jenkyn et al. and Linden resulted in reports of increased stiffness in the transverse direction, and as such it was seen fitting to determine the coefficients of the equations presented based on our results for further validation. In this work we slightly refined Equation 2 by considering two different k parameters, k_1 and k_2, in the cross fiber and fiber directions, respectively. The hyperelastic parameters were determined through nonlinear optimization using data generated by the proposed computational model. For this purpose, the nonlinear least squares optimization algorithm in MATLAB (MATLAB 9.3 and Optimization Toolbox 9.3, The MathWorks, Inc., Natick, Massachusetts, United States) was utilized.

2.2.7 Validation

The model's mechanical properties in both fiber and cross fiber directions are compared to the passive tensile mechanical testing performed on fresh porcine skeletal muscle. Porcine tissues are known to resemble human tissues while their experimental data is available[84]. The coefficients for the strain energy density equations presented earlier are also determined using their derivatives and our models stress-strain relationships through a non-linear least squares optimization.

2.3 « Results »

2.3.1 ECM Part Modelling

Using the Yeoh model's hyperelastic parameters of mitochondria as well as the available experimental data of collagen and fat, the ECM stress-strain curve was obtained from a

uniaxial extension of the cylindrical sample and is shown in Figure 2-3(a). The relative volume percentages of each constituent used in this cylindrical sample FE model are given in Table 2-1.
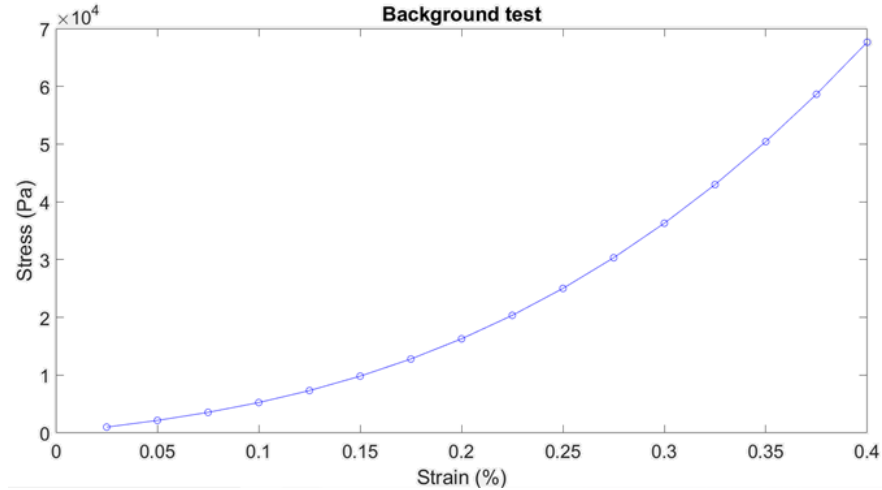
Figure 2-4 Simulated stress-strain curve of ECM part for normal skeletal muscle tissue.

3.2 Normal Skeletal Muscle Modelling and Case Studies

We used data we generated from the ECM simulation in the previous part to construct FE model of normal skeletal muscle. Using this model, uniaxial extensions of the constructed skeletal muscle tissue model were simulated in fiber and across fiber directions. Resulting stress-strain relations are illustrated in Figure 2-5(a) and (b) that demonstrate the data in fiber and cross fiber directions, respectively. These figures also show corresponding experimental stress-strain data of fresh porcine skeletal muscle as reported by Takaza et al[57]. Ad-hoc optimization of Z-disc in the model led to a Neo-Hookean hyperelastic parameter C_1 value of 15 MPa. This may be regarded as the first estimate of hyperelastic parameter of intact *ex vivo* Z-discs. The figures illustrate stress-strain data generated for low, medium and high myofiber content cases, by altering the volume percentages of myofiber to 82%, 90% and 98%. They consistently indicate higher stiffness characteristics with increased muscle fiber volume percentage. Results of the spastic case study is also

illustrated in this figure (red-line) which shows drastic reduction in stiffness compared to normal skeletal muscle. This is consistent with the data presented by Lieber et al[47].
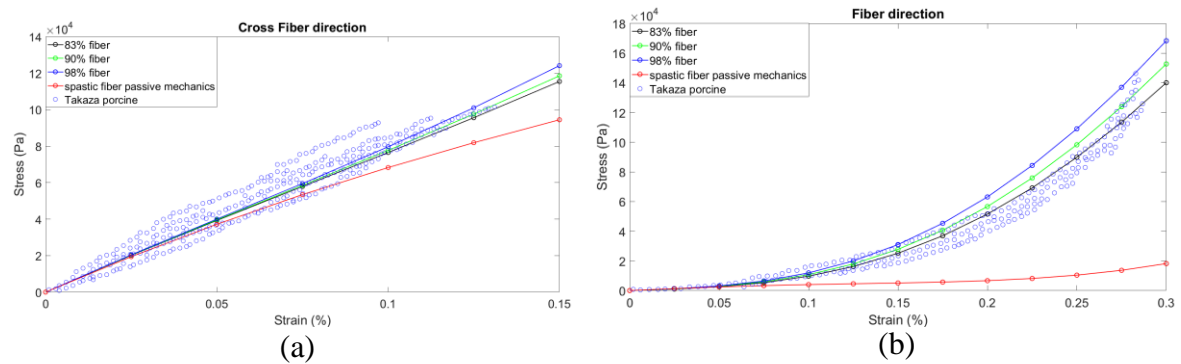
Figure 2-6 Stress-strain curves of simulated skeletal muscle tissue behaviour along fiber direction (a) and cross-fiber direction (b) obtained from uniaxial FE simulations are shown and compared to recently published data of fresh porcine skeletal muscle stress-strain experimental scatter points (blue). Solid black, green, and blue line stress-strain results correspond to 82%, 90%, and 98% muscle fiber volume percentages in the whole muscle tissue, respectively. Solid red lines show the predicted stress-strain relationship corresponding to spastic muscle.

2.3.2   Sensitivity Analysis

The volume percentages of background tissue constituents were altered as aforementioned. The simulated ECM test data was used as input data for the whole tissue modelling following a Yeoh hyperelastic fitting. Myofibrils were treated similarly as for normal skeletal muscle tissue. Uniaxial test simulations lead to sensitivity results shown in Table 2-3 corresponding to along and across fiber directions as previously described.

Table 2-2 Along-fiber and Cross-fiber instantaneous moduli changes (kPa) are reported for the three selected strain regimes per each direction as a result of 2% change in each ECM constituent volume. The percent change in the Young's moduli are also reported.

	Along-fiber	Cross-fiber	Along-fiber	Cross-fiber	Along-fiber	Cross-fiber

Strain	10%	5%	20%	10%	30%	15%
Collagen	209.9 (0.04%)	283.6 (0.52%)	1111.5 (0.04%)	943.9 (0.88%)	2359.8 (0.03%)	2287.1 (1.39%)
Fat	-13.2 (-0.003%)	-2.61 (-0.005%)	5.82 (0.00024%)	-10.83 (-0.01%)	101.5 (0.001%)	65.8 (0.04%)
Mitochondria	-69.2 (-0.01%)	-96.37 (-0.18%)	-379.62 (-0.014%)	-319.8 (-0.30%)	-821.6 (-0.011%)	-790.7 (-0.48%)

2.3.3   Anisotropic Hyperelastic Model Parameters of Passive Skeletal Muscle

The nonlinear least squares optimization led to the determination of the coefficients shown in Table 2-4.

Table 2-3 Anisotropic hyperelastic parameters obtained using our proposed model data and corresponding parameters reported based on the experimental works of Jenkyn and Linden for rabbit and rat, respectively.

	a_1	k_1	a_2	k_2
Coelho et al.	6.8	0.98	6.2	0.11
Jenkyn et al.	8	0.05	6	0.05
Linden	2.5	0.01	1	0.01

2.4 « Discussion »

This paper presents a micro-to-macro method for modelling the intrinsic properties of skeletal muscle tissue. It follows the structural approach of tissue mechanics modeling and utilizes the FE method for implementation where the tissue ultrastructural constituents are considered to capture the tissue's intrinsic mechanical properties. This accounts for the nonlinearity and anisotropy of skeletal muscle using the appropriate constituent volumes, their distributions and intrinsic properties noting that the macroscopic mechanical characteristics of the tissue is shaped by the volume percentage, distribution, and mechanical properties associated with its microstructural constituents. Using estimations for normal skeletal muscle tissue composition and associated microstructural mechanical properties, simulations lead to a good agreement with recent experimental data of uniaxial testing performed on fresh porcine skeletal muscle[57]. A similar trend between fiber and cross-fiber mechanical behaviour can be seen in other works including fresh rabbit skeletal muscle experimentation[85]. It is important that comparisons be made with fresh skeletal muscle tissue samples to avoid the stiffening effects of rigor-mortis. Using an ad hoc approach to estimate the Z-disc mechanical properties, the Neo Hookean parameter C_1 was estimated at 15 MPa leading to a good agreement between simulated tissue and experimental findings for both along and across fiber orientations. Compared to variable reports that attempt to quantify the mechanical behaviour of the skeletal muscle Z-discs using atomic force microscopy, our model predicts a Young's modulus of approximately 90 MPa while assuming tissue incompressibility[36,61,62]. While it may be regarded as the first estimate for intact *ex vivo* Z-discs, this estimate is higher than measurements obtained using atomic force microscopy. The measurement difference could be attributed to actomyosin slippage and other elastic contributions involved in atomic force microscopy which lead to stiffness underestimation. Rigorous sample preparation required for atomic force microscopy may also lead to a greater disintegration of the tissue compared to whole tissue experimental testing. Due to the complex microstructure of myofibrils, atomic force microscopy presumably quantifies the more compliant apparent modulus due to localized plastic deformations in the material[62]. As predicted, the incorporation of these stiffer regions leads to an elevated stiffness transverse to the myofibril direction.

As previously mentioned, various pathologies can lead to significant alterations in the microstructural composition and mechanical properties of skeletal muscle. Aging and exercise levels for example can influence the myofibrillar volume, presence of muscular fat, and mitochondrial volume. Features such as these can easily be captured in the model by making simple modifications to the appropriate constituent volume percentages[72,81]. Aging is also known to increase the stiffness of the extracellular matrix due to extensively crosslinked collagen[82]. Phenomenon that alter the specific mechanical properties of a constituent can easily be modelled by appropriately modifying the mechanical inputs of the model. The case study presented in this article demonstrated the altered passive tensile mechanics as a result of changing the muscle fiber volume percentage as well as altering myofibril bundle mechanics. Leiber et al. found that the tangent modulus of spastic muscle bundles was less than one quarter to that of normal muscle bundles, however, more accurate passive modelling of spastic muscle would require research elucidating its possible effects on Z-discs and the ECM for incorporation in our model[47].

The diaphragm is a skeletal muscle and has been reported to undergo muscle fiber type transformation resulting from COPD. Furthermore, the myofibrillar titin molecule is more extensible in COPD muscle. Characteristics including fiber type transformation and titin extensibility because of COPD would directly affect the predicted Z-disc volume percentage. This can be attributed to the fact that in COPD fast twitch fibers have narrower Z-bands while myofibril mechanical properties are altered. Biomechanical models for the diaphragm are being developed to aid in tumour motion compensation for lung cancer treatment[86]. Incorporating such alterations through the proposed model may lead to furthering the realism of diaphragmatic skeletal tissue modelling, hence improving the accuracy of lung tumor compensation and leading to better lung cancer treatment outcome.

Each constituent and their associated mechanical properties, volume, and distribution is adaptive in this model to characterize specific skeletal muscle tissue related to its structure. The adaptability of the model was explored through the presented sensitivity analysis. Alterations in the ECM constituent volume percentages resulted in a newly predicted whole tissue mechanical behaviour. Sensitivity results showed that alterations in volume percentages can have a different impact on the overall tissue characteristics at different

tensile strains. As would be expected, with a greater presence of collagen, the tissue model becomes increasingly stiff at larger strains as seen in Table 2-3. Morphometric studies determining the composition of tissue should be more attuned when quantifying collagen compared to other constituents due to its relatively high sensitivity towards affecting the overall mechanics of the tissue. As more information is uncovered regarding skeletal muscle morphology and micromechanical alterations as a result of pathology, the model could be further tested for validity and adaptability.

As aforementioned, discrepancies exist among stress-strain data obtained by different investigators for skeletal muscle tissue in fiber and cross fiber directions. However, it has been consistently shown that the cross-fiber direction exhibits a stiffer and generally more linear trend in the case of experimental testing on fresh and *in-vivo* tissue samples[84,83,56,31]. The following Figure 2-7(a) and (b) are extensions of Figure 2-5(a) and (b) to include the fittings obtained based on the strain energy density equation introduced in Section 2.5. While Jenkyn et al. fit the model to rabbit experimental data we used our simulation data to determine the model's coefficients. Disparities seen between researcher's experimental data are not uncommon, Takaza and Nie porcine experimental data have been found to mainly disagree in the along fiber direction, which are expected to be due to experimental protocol. The dynamic high strain rate testing used by Nie may have accelerated the process of rigor-mortis which has been shown to increase the stiffness and linearity of the tissue mechanical behaviour in the along the fiber direction[31]. The results from Jenkyn et al. are shown because their works used data collected from *in vivo* experiments on rabbits to determine the muscle tissue anisotropic hyperelastic parameters. The coefficients we determined based on our simulation seen in Table 2-4 are compared to that of the work performed by Jenykns et al. and Linden. The constants a1 and a2 describe the passive stiffness in the perpendicular and parallel fiber directions, respectively. The elevated stiffness transverse to fibers is reflected in the values of a and k which are larger for the cross fiber direction. The k parameter is related to the initial stiffness of the material whereas the a value related to the passive stiffness of the corresponding direction. Previously, a single k value was determined which assumes the same initial stiffness in both directions. We did not make this assumption and determined separate k values for each direction. The main discrepancy seen between the model fitting and our simulated

data is found at increasing strains in the cross-fiber direction. Similarly, Jenkyn et al. found that the model deviated from the true stress-strain relation at high strains which they attributed to possible tissue damage. Our model incorporates Z-discs which tend to dominate the transverse stiffness of the tissue model, alleviating the stress-stiffening response seen with the model fitting.

a)

b)
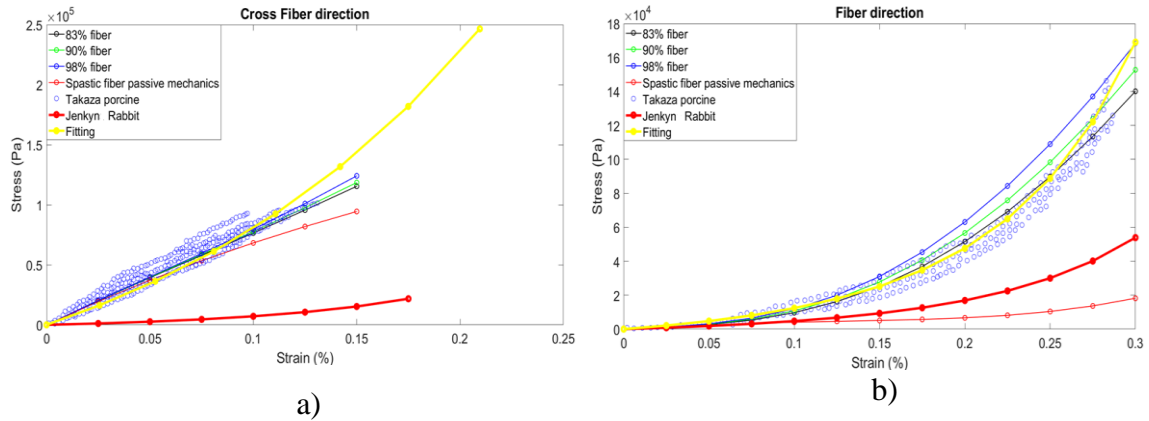
Figure 2-8 Stress-strain curves of simulated skeletal muscle tissue behaviour along fiber direction (a) and cross-fiber direction (b) obtained from uniaxial FE simulations are shown and compared to Takaza's fresh porcine skeletal muscle stress-strain experimental scatter points (blue). Solid black, green, and blue line stress-strain results correspond to 82%, 90%, and 98% muscle fiber volume percentages in the whole muscle tissue, respectively. Thin red lines show the predicted stress-strain relationship corresponding to spastic muscle. Results from Jenkyn et al. fittings are shown in thick red lines.

2.5 « Conclusions »

The major advantage of the proposed tissue modelling approach is its flexibility and ability to mimic diverse skeletal muscle characteristics. Generally, this would be as simple as modifications to the volume percentages of tissue constituents depending on the morphology. The model could also be adapted to micromechanical alterations as well as

the distribution of constituents. As such, it can be employed as a computer simulator to catalogue the mechanical properties of various healthy and pathological skeletal muscles. The advent of modelling the lattice structured Z-discs in the model allowed for a satisfying capture of the along and across-fiber tissue mechanical properties, which is an essential characteristic for clinical skeletal muscle tissue modelling. The decomposition of the tissue into constituents is an extension of the renowned Hill's model composite. The model's adaptability is further explored through considering the altered mechanical characteristics of spastic muscle fiber bundles. It is important that the model input parameters including volume percentages and mechanical properties are accurate in order achieve the most accurate skeletal muscle tissue model.

2.6 « References »

1.   Röhrle O, Davidson JB, Pullan AJ. A physiologically based, multi-scale model of skeletal muscle structure and function. Front Physiol. 2012;3:358.

2.   Mathur S, Brooks D, Carvalho CRF. Structural alterations of skeletal muscle in copd. Front Physiol. 2014;5:104.

3.   Van Naarden Braun K, Doernberg N, Schieve L, Christensen D, Goodman A, Yeargin-Allsopp M. Birth Prevalence of Cerebral Palsy: A Population-Based Study. Pediatrics. 2016;137(1):1.

4.   Rizzo MA, Hadjimichael OC, Preiningerova J, Vollmer TL. Prevalence and treatment of spasticity reported by multiple sclerosis patients. Mult Scler J. 2004;10(5):589-595.

5.   Lieber RL, Runesson E, Einarsson F, Fridén J. Inferior mechanical properties of spastic muscle bundles due to hypertrophic but compromised extracellular matrix material. Muscle Nerve. 2003;28(4):464-471.

6.   Stylianopoulos T, Barocas VH. Volume-averaging theory for the study of the mechanics of collagen networks. Comput Methods Appl Mech Eng. 2007;196(31):2981-2990.

7.   Myers KM, Hendon CP, Gan Y, et al. A continuous fiber distribution material model for human cervical tissue. J Biomech. 2015;48(9):1533-1540.

8.   Haddad SMH, Samani A. A computational model of the left ventricle biomechanics using a composite material approach. Int J Eng Sci. 2017;111:61-73.

9.   Driessen NJB, Bouten CVC, Baaijens FPT. A structural constitutive model for collagenous cardiovascular tissues incorporating the angular fiber distribution. J Biomech Eng. 2005;127(3):494-503.

10.   Barocas VH, Tranquillo RT. An anisotropic biphasic theory of tissue-equivalent mechanics: the interplay among cell traction, fibrillar network deformation, fibril alignment, and cell contact guidance. J Biomech Eng. 1997;119(2):137-145.

11.   Mow VC, Kuei SC, Lai WM, Armstrong CG. Biphasic Creep and Stress Relaxation of Articular Cartilage in Compression: Theory and Experiments. J Biomech Eng. 1980;102(1):73.

12.   Hill MR, Simon MA, Valdez-Jasso D, Zhang W, Champion HC, Sacks MS. Structural and Mechanical Adaptations of Right Ventricle Free Wall Myocardium to Pressure Overload. Ann Biomed Eng. 2014;42(12):2451-2465.

13.   Bell RD, MacDougall JD, Billeter R, Howald H. Muscle fiber types and morphometric analysis of skeletal muscle in six-year-old children. Med Sci Sports Exerc. 1980;12(1):28-31.

14.   Yoshikawa Y, Yasuike T, Yagi A, Yamada T. Transverse Elasticity of Myofibrils of Rabbit Skeletal Muscle Studied by Atomic Force Microscopy. Biochem Biophys Res Commun. 1999;256(1):13-19.

15.   Ogneva I V, Lebedev D V, Shenkman BS. Transversal stiffness and Young's modulus of single fibers from rat soleus muscle probed by atomic force microscopy. Biophys J. 2010;98(3):418-424.

16.   Nie X, Cheng J-I, Chen WW, Weerasooriya T. Dynamic Tensile Response of Porcine Muscle. J Appl Mech. 2011;78(2):21009.

17.   Morrow DA, Haut Donahue TL, Odegard GM, Kaufman KR. Transversely isotropic tensile material properties of skeletal muscle tissue. J Mech Behav Biomed Mater. 2010;3(1):124-129.

18.   Odegard GM, Donahue TLH, Morrow DA, Kaufman KR. Constitutive modeling of skeletal muscle tissue with an explicit strain-energy function. J Biomech Eng. 2008;130(6):61017.

19.   Takaza M, Moerman KM, Gindre J, Lyons G, Simms CK. The anisotropic mechanical behaviour of passive skeletal muscle tissue subjected to large tensile strain. J Mech Behav Biomed Mater. 2013;17:209-220.

20.   Wheatley BB, Odegard GM, Kaufman KR, Donahue TLH. How does tissue preparation affect skeletal muscle transverse isotropy? J Biomech. 2016;49(13):3056-3060.

21.   Sokolis DP. Passive mechanical properties and constitutive modeling of blood vessels in relation to microstructure. Med Biol Eng Comput. 2008;46(12):1187-1199.

22.   Dagan D, Be'ery M, Gefen A. Single-trabecula building block for large-scale finite element models of cancellous bone. Med Biol Eng Comput. 2004;42(4):549-556.

23.   Haddad SMH, Samani A. A novel micro-to-macro approach for cardiac tissue mechanics. Comput Methods Biomech Biomed Engin. 2017;20(2):215-229.

24.   Ogneva I V, Lebedev D V, Isaev-Ivanov V V, Shenkman BS. [Spatial distribution of transverse stiffness of relaxed and activated rat soleus myofibers]. Biofizika. 53(6):1073-1077.

25.   Ogneva I V, Lebedev D V, Shenkman BS. Transversal stiffness and Young's modulus of single fibers from rat soleus muscle probed by atomic force microscopy. Biophys J. 2010;98(3):418-424.

26.   Transverse Elasticity of Myofibrils of Rabbit Skeletal Muscle Studied by Atomic Force Microscopy. Biochem Biophys Res Commun. 1999;256(1):13-19.

27.   Hoppeler H, Luthi P, Claassen H, Weibel ER, Howald H. The ultrastructure of the normal human skeletal muscle. Pflugers Arch Eur J Physiol. 1973;344(3):217-232.

28.   Power GA, Dalton BH, Rice CL. Human neuromuscular structure and function in old age: A brief review. J Sport Heal Sci. 2013;2(4):215-226.

29.   Rice CL, Cunningham DA, Paterson DH, Lefcoe MS. Arm and leg composition determined by computed tomography in young and elderly men. Clin Physiol. 1989;9(3):207-220.

30.   Overend TJ, Cunningham DA, Paterson DH, Lefcoe MS. Thigh composition in young and elderly men determined by computed tomography. Clin Physiol. 1992;12(6):629-640.

31.   Gillies AR, Lieber RL. Structure and function of the skeletal muscle extracellular matrix. Muscle Nerve. 2011;44(3):318-331.

32.   Luther PK, Padrón R, Ritter S, Craig R, Squire JM. Heterogeneity of Z-band Structure Within a Single Muscle Sarcomere: Implications for Sarcomere Assembly. J Mol Biol. 2003;332(1):161-169.

33.   Burgoyne T, Morris EP, Luther PK. Three-Dimensional Structure of Vertebrate Muscle Z-Band: The Small-Square Lattice Z-Band in Rat Cardiac Muscle. J Mol Biol. 2015;427(22):3527-3537.

34.   Polla B, D 'antona G, Bottinelli R, Reggiani C. Respiratory muscle fibres: specialisation and plasticity. Thorax. 2004;59:808-817.

35. Levine S, Kaiser L, Leferovich J, Tikunov B. Cellular Adaptations in the Diaphragm in Chronic Obstructive Pulmonary Disease. N Engl J Med. 1997;337(25):1799-1806.

36. Karjalainen J, Tikkanen H, Hernelahti M, Kujala UM. Muscle fiber-type distribution predicts weight gain and unfavorable left ventricular geometry: a 19 year follow-up study. BMC Cardiovasc Disord. 2006;6:2.

37. Orozco-Levi M, Gea J, Lloreta J, et al. Subcellular adaptation of the human diaphragm in chronic obstructive pulmonary disease.

38. Kiessling K-H, Pilstrum L, Karlsson " A N J, Piehl IN. Mitochondrial volume in skeletal muscle from young and old physically untrained and trained healthy men and from alcoholics. Clin Sci. 1973;44:547-554.

39. Tam CS, Covington JD, Bajpeyi S, et al. Weight gain reveals dramatic increases in skeletal muscle extracellular matrix remodeling. J Clin Endocrinol Metab. 2014;99(5):1749-1757.

40. Physiological Society (Great Britain). Meeting. T, Isaka T, Fujita S, Hamaoka T. Proceedings of the Physiological Society. Physiological Society; 2006.

41. Zhu R, Wen C, Li J, Harris MB, Liu Y-Y, Kuo C-H. Lipid storage changes in human skeletal muscle during detraining. Front Physiol. 2015;6:309.

42. Roeder BA, Kokini K, Sturgis JE, Robinson JP, Voytik-Harbin SL. Tensile mechanical properties of three-dimensional type I collagen extracellular matrices with varied microstructure. J Biomech Eng. 2002;124(2):214-222.

43. Alkhouli N, Mansfield J, Green E, et al. The mechanical properties of human adipose tissues and their relationships to the structure and composition of the extracellular matrix.

44.   Seyfi B, Sabzalinejad M, Haddad SMH, Fatouraee N, Samani A. A FSI-based structural approach for micromechanical characterization of adipose tissue. In: Krol A, Gimi B, eds. International Society for Optics and Photonics; 2017:101370G.

45.   Safshekan F, Tafazzoli-Shadpour M, Abdouss M, Shadmehr MB. Mechanical Characterization and Constitutive Modeling of Human Trachea: Age and Gender Dependency. 2016.

46.   Meyer GA, Lieber RL. Elucidation of extracellular matrix mechanics from muscle fibers and fiber bundles. J Biomech. 2011;44(4):771-773.

47.   Deschenes MR. Effects of aging on muscle fibre type and size. Sports Med. 2004;34(12):809-824.

48.   Volpi E, Nazemi R, Fujita S. Muscle tissue changes with aging. Curr Opin Clin Nutr Metab Care. 2004;7(4):405-410.

49.   Marcus RL, Addison O, Kidde JP, Dibble LE, Lastayo PC. Skeletal muscle fat infiltration: impact of age, inactivity, and exercise. J Nutr Health Aging. 2010;14(5):362-366.

50.   Menshikova E V, Ritov VB, Fairfull L, Ferrell RE, Kelley DE, Goodpaster BH. Effects of exercise on mitochondrial content and function in aging human skeletal muscle. J Gerontol A Biol Sci Med Sci. 2006;61(6):534-540.

51.   Berria R, Wang L, Richardson DK, et al. Increased collagen content in insulin-resistant skeletal muscle. AJP Endocrinol Metab. 2005;290(3):E560-E565.

52.   Jenkyn TR, Koopman B, Huijing P, Lieber RL, Kaufman KR. Finite element model of intramuscular pressure during isometric contraction of skeletal muscle. Phys Med Biol. 2002;47(22):4043-4061.

53.   Linden BJJJ van der. Mechanical modeling of skeletal muscle functioning. May 1998.

54.   Takaza M, Moerman KM, Gindre J, Lyons G, Simms CK. The anisotropic mechanical behaviour of passive skeletal muscle tissue subjected to large tensile strain. J Mech Behav Biomed Mater. 2013;17:209-220.

55.   Jannapureddy SR, Patel ND, Hwang W, Boriek AM. Selected Contribution: Merosin deficiency leads to alterations in passive and active skeletal muscle mechanics. J Appl Physiol. 2003;94(6).

56.   Coelho B, Karami E, Haddad SMH, Seify B, Samani A. A biomechanical approach for in vivo diaphragm muscle motion prediction during normal respiration. In: Webster RJ, Fei B, eds. International Society for Optics and Photonics; 2017:1013505.

Chapter 3

3 « Micromechanics Based Modelling of in-vivo Respiratory Motion of the Diaphragm Muscle »

3.1 « Introduction»

The respiratory system in humans is a vital and complex arrangement of structures and organs that work together to generate pressure variations in the lung allowing for air flow in and out of the lung, leading to oxygen exchange. Computational modelling of such a system has become increasingly popular as our understanding of their underlying science increases and relevant technology becomes available. Respiratory computational models are valuable in that they provide insight into the complicated physiology and may provide aid in diagnosis and treatment for respiratory diseases and management, respectively. The major driver of respiratory motion is the diaphragm muscle, especially when considering normal shallow breathing. Existing lung and respiratory models are generally driven by estimated pressure variations and prescribed boundary conditions that are often attained through image registration techniques[1,2,3]. Such simplifications do not model the respiratory motion based on comprehensive model of physiological behaviour, which can lead to inaccuracies. Lung deformation during respiration, which are mainly concentrated at the lower lobes of the lung, is mainly due to muscle contractions of the diaphragm muscle[3]. This has led to biomechanical modelling of the diaphragm, which can ultimately be incorporated into respiratory models of increasing complexity. Further to gaining insights related to the diaphragm physiology, biomechanical modelling of respiration can also aid in treatment for respiratory diseases such as lung cancer which involves reliable prediction of tumour motion during breathing[4]. Lung cancer has proven to be the deadliest among all cancers. Radiation therapy is known to be the most effective method for treating this disease. However, tumour motion compensation, which is required for effective treatment, remains an outstanding concern. Lung tumour motion is generally clinically significant and if not accounted for properly, the effectiveness of radiotherapy can degrade considerably. Common methods for motion compensation include image guided techniques and computer assisted techniques such as lung biomechanical model based techniques. During inhalation, the diaphragm muscle

contracts while the rib cage expands, leading to generation of the thoracic pressure variations associated with diaphragm and lung deformation. Diaphragm motion has been shown to function as an anatomic surrogate for lung tumour motion[5]. Image guided motion compensation techniques often use a combination of rigid and non-rigid registrations, however due to large deformations and non-physical based assumptions, predicted deformation fields can be inaccurate. Furthermore, image guided techniques often require repeated 4D-CT scans in order to estimate tumour motion, which is harmful to the patient. The purpose of this work is to construct a biomechanically accurate FE model to capture the deformations of the diaphragm muscle during respiration. Existing FE-models[6,7,8,9,10] develop a diaphragm mesh based on image segmentations and assign muscle and tendon regions which includes the addition of myofibers according to the physiology of the diaphragm muscle in order to contract. Some models are over simplified to treat the muscle like a piston in that contraction forces act only in the superior-inferior direction[11]. For biomechanical modelling of muscle tissue, important features include the geometry, tissue mechanical properties, boundary conditions, and loading. In general, model geometries are attained through segmentation of CT images. The mechanics and transverse isotropy are captured using hyperelastic transversely isotropic strain energy functions following[6]:

$$U_I = ce^{b\left(\bar{I}_1^C - 3\right) - 1} \tag{1}$$

$$U_f\left(\bar{\lambda}_f, \alpha, \gamma\right) = U_{PE}\left(\bar{\lambda}_f\right) + U_{CE}\left(\bar{\lambda}_f, \alpha, \gamma\right) \tag{2}$$

where U_I and U_f are the strain energies stored in the isotropic hyperelastic extracellular matrix and muscle fiber, respectively. c and b are material constants, λ_f is the stretch ratio in the fiber direction, γ is the activation level of the muscle which varies from 0 to 1, α represents the time dependence of the activation and I_1 is the first invariant of the Cauchy-Green deformation tensor. Muscle tissue can be modeled using the well-known Hill's model. The active element in this model leads to the development of internal stress leading to contraction of both the passive and active components due to bonding. The

passive component represents the extracellular matrix and the contractile and elastic elements relate to the muscle fibers active and passive mechanics, respectively. The total muscle force F is a sum of the forces in the elements where

$$F = \mathrm{F}^{PE} + \mathrm{F}^{EE} = \mathrm{F}^{PE} + \mathrm{F}^{CE} \tag{3}$$

PE, EE, and CE represent passive elements, contractile elements, and elastic elements, respectively. The total force corresponds to the nominal stress along the fiber direction. The passive stress T^{PE} is usually defined as follows:

$$T^{PE} = T_0^M f_{PE}(\lambda_f) \tag{4}$$

Where T_0^M denotes the maximum muscle stress which in turn determines the maximum contraction force. λ_f is the stretch ratio in the fiber direction. f_{PE} is the passive force-length relation given by:

$$f_{PE}(\lambda_f) = 2aA(\lambda_f - 1)e^{a(\lambda_f - 1)^2}, \text{for } \lambda_f > 1 \tag{5}$$

Where a and A are material constants, and $f_{PE} = 0$ if λ_f is equal to or less than 1. The active stress T^{CE} is given by

$$T^{CE} = T_0^M f_{CE}(\lambda_f)\alpha(t)\gamma \tag{6}$$

where γ is the activation level of the muscle from 0 to 1, α represents the time dependence of the activation, and $f_{AE}(\lambda_f)$ is the active force-length relation in the active element. According to experimental data from an adult baboon[12], the force-length relationship of the diaphragm muscle is

$$f_{CE}^{Dia}\left(\lambda_f\right) = \begin{cases} 1.80\lambda_f - 0.80, & \text{for } 0.6 \leq \lambda_f < 0.7 \\ 2.37\lambda_f - 1.20, & \text{for } 0.7 \leq \lambda_f < 0.8 \\ 1.61\lambda_f - 0.59, & \text{for } 0.8 \leq \lambda_f < 0.9 \\ 1.42\lambda_f - 0.42, & \text{for } 0.9 \leq \lambda_f < 1.0 \\ -0.55\lambda_f + 1.55, & \text{for } 1.0 \leq \lambda_f < 1.1 \\ -2.11\lambda_f + 3.27, & \text{for } 1.1 \leq \lambda_f < 1.2 \\ 0, & \text{otherwise} \end{cases}$$

The time dependence of the muscle activation α(t) was fit to experimental data obtained from dogs[13]. Pato et al. used a similar approach which also mimics the time-dependent activation process for the contractile element which is a result of neural excitation[9]. The first order ordinary differential equation (ODE) was proposed by Pandy et al[14]. Modelling muscle in conjunction with the aforementioned strain energy density equations related to the extracellular matrix and muscle fibers, the active and passive stress-strain relationship of the muscle can be achieved. Further to the internal forces generated within the diaphragm muscle, abdominal and pleural pressures act on the upper surface of the diaphragm and inner surface of the thorax, respectively. Inner thorax pressure variations that occur with normal breathing range from approximately -0.5 to -0.75kPa[15]. Contact forces and pressures acting on the lower surface of the diaphragm are difficult to obtain and can be non-uniform due to the presence of organs and friction[16]. Abdominal pressure variations approximate these forces and have been estimated to range from 0 to 2kPa.

Novelties of the proposed technique of modelling the diaphragm include a unique way of defining muscle fiber direction according to physiology, the incorporation of musculoskeletal Z-disk mechanics which plays an important role in capturing transverse isotropy of the tissue, and a micro-to-macro mechanical approach for the model's adaptable mechanical properties. The skeletal diaphragm model is modelled following the Hill's model where we use an alternate approach of utilizing rebar layers embedded in the finite elements. Rebar layers are used to simulate the fiber bundles within the muscle tissue or rather, extracellular matrix. Rebar layers can be distributed throughout elements

with their own associated volume and orientation. Rebars can have specific mechanical properties that are different from the element tissue. Their utility serves to model myofiber bundles found in the extracellular matrix of skeletal muscle. This allows for local definition of myofiber direction, generation of myofiber bundle to ECM ratio consistent with muscle morphometry, leading to a self-contained anisotropy. This model can be developed and solved within off the shelf FE software packages such as Abaqus (Dassault Systèmes Simulia Corp., Providence, RI, USA). Prestress is applied linearly to the rebar in order to simulate contraction forces. The contraction forces in our diaphragm model are optimized in order to predict their magnitudes. The performance of the model for normal respiration is evaluated based on matching geometrical configuration of patient's contracting diaphragms obtained via imaging. Moreover, the diaphragm is considered under the pathological condition of unilateral paralysis in order to study the disease and demonstrate the adaptability of the model.

3.2 « Materials and Methods »

3.2.1 Data Acquisition and Diaphragm Segmentation

The 3-D CT images used in this study for developing diaphragm models correspond to the end exhalation phase of four-dimensional 4-D CT datasets acquired from the thorax and abdomen of three cancer patients. The patients were scanned using a 16-slice Philips Brilliance Big Bore CT scanner (Philips Medical Systems, Cleveland, United States) functioning in helical mode. Scanning parameters include 120 kVp and 400 mAs⁄slice for tube potential and current, respectively. The pitch of the couch depends on the patient's breathing period and it was set to approximately 0.1. The intraslice pixel size of the data varied from 0.98 to 1.29 mm while superior-inferior slice thickness was 3 mm. The 4-D CT images were divided into 10 respiratory phases using real-time position management™ system.

3.2.2 FEM of the diaphragm

The development of a patient specific model of the diaphragm muscle began with modification and use of a previously developed automatic segmentation algorithm for 4D-CT images in order to segment the diaphragm volume at end exhalation, which coincides with muscle relaxation[17]. The diaphragm volume was converted into a mesh with hexahedral elements using 3D slicer. Due to the lack of contrast in the CT images, the diaphragm volume was converted into a thin surface based on image information and an average diaphragm muscle thickness of approximately 4 mm[10,18,19] was considered. The diaphragm was assigned a central tendon region according to average surface area measures of approximately 143 cm^2 using a trefoil shape positioned slightly anteriorly as described in humans[20]. The remaining elements serve as to model the diaphragm muscle tissue.

Muscle elements of the diaphragm are modelled according to the well-established Hill's model which contains both an active component and passive component where rebars are installed into elements in order to act as myofibers. The rebars can be prestressed in order to simulate the myofibers active contraction while the remaining volume behaves passively, much like the extracellular matrix. Contraction in both components is achieved because all parts are bonded and equilibrium is maintained. When the diaphragm is relaxed, myofibers radiate from the central tendon and extend towards the muscles outer attachments while following the curvature of the tissue[16,21,18,22]. Muscle fibers in outer regions run mainly along the craniocaudal axis[23]. The crural region is known to have a more complex orientation of fibers that allow it to act as a sphincter during specific bodily functions, however, for the purpose of modelling normal respiration, detailed modeling of that region was not deemed necessary[24]. Vectors radiating from the hemidiaphragm dome peaks were projected onto the outer surface of each element. The projections determined the direction of rebar installments in order to satisfy the aforementioned physiology of the diaphragm muscle. The percent volume of rebar installed is input according to normal measures of myofiber to extracellular matrix ratios found in skeletal muscle[25,26]. The final component used in modelling the muscle tissue involved the installment of Z-disk regions, which according to the tissue model presented in Chapter 2, accounts for the transverse

isotropy of the tissue[27,28,29]. This was done with embedded elements and using a percentage volume according to the diaphragm muscle fiber type composition determined in the previously mentioned work. Figure 1 is a visual representation of how rebar and embedded elements were incorporated into finite elements. Z-disk regions are resolved for each element and are embedded transversely to myofibers while having their own associated mechanics as previously determined in Chapter 2.
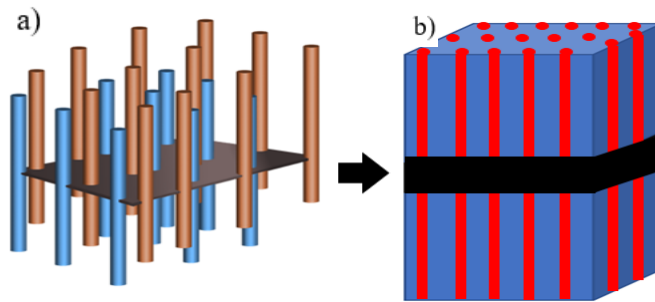
Fig. 1. a) shows the Z-disk region as a black plane traversing actin filaments originating from adjacent sarcomeres coloured red and blue. b) shows how the Z-disks were modelled using a FE scheme in the proposed model where red rebars can be varied in area and number to model myofibers in background tissue.

The central tendon, rebars, extracellular matrix, and embedded elements each have specific mechanical properties assigned. The central tendon, which is virtually inextensible under normal physiological breathing, was modelled as a linear elastic material with a Young's modulus of 33 MPa[10,21]. The rebar and ECM parts were modelled using the Yeoh hyperelastic model. Details can be found in Chapter 2. This approach is suitable for large deformations and the intrinsically nonlinear mechanical nature of the tissue. Stress-strain experimental data for skeletal muscle fiber bundles was attained from literature which was fitted to the Yeoh model and assigned as rebar mechanical properties[30]. The element volume surrounding the rebar acts as the ECM. This part was initially modelled using a micro-to-macro mechanical approach using a cylinder sample containing appropriate amounts of mitochondria, fat, and collagen[31]. The cylinder underwent uniaxial testing in order to generate the stress-strain relation for

the modelled ECM, which was also fit to the Yeoh hyperelastic model. The Z-disks, which have been shown to increase lateral stiffness, were assigned mechanical properties based on the aforementioned previous work. The Z-disk properties were optimized such that the modelled muscle tissue best matched the transverse isotropy of whole skeletal muscle tissue. The Z-disks were modelled using the Neo-Hookean hyperelastic model with a C_1 value of 15 MPa. The volume percentages of each constituent can be modified allowing for adaptable mechanics, if specific morphometric information is estimated for each patient. Figure 2 shows the cylindrical and slab models used to model the extracellular matrix and whole muscle tissue as per the description given in Chapter 2.

a) b)
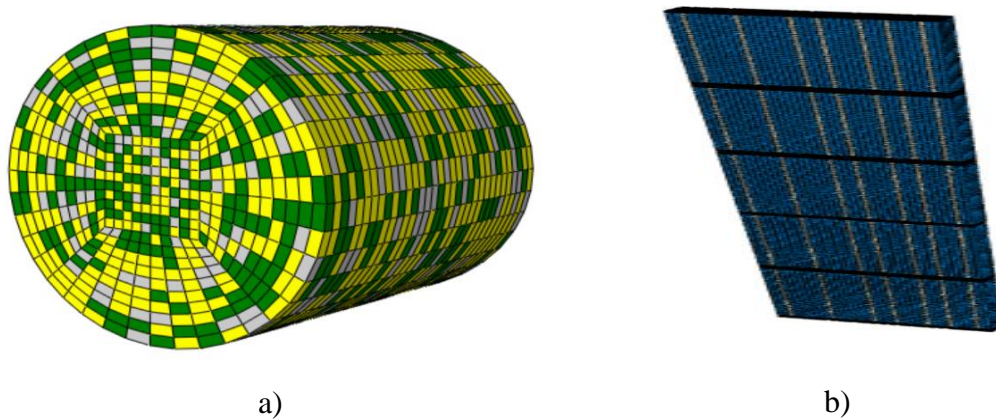
Fig. 2. FE model of (a) cylindrical sample of ECM part composed of adjustable amounts of mitochondrion (green), fat (yellow), and collagen (grey) and (b) slab sample of whole skeletal muscle tissue composed of adjustable amounts of ECM (white), muscle fiber bundles (blue) and Z-disk elements (black).

The model's boundary conditions has two major distinct assignments based on physiology and information attained via 4D-CT image registrations. The diaphragm muscle attaches inferiorly to the lower ribs, posteriorly to the lower lumbar vertebrae, and anteriorly to the xiphoid process. Nodes found in the lower region closest to the lumbar vertebrae were set as fixed, because the spine is rigid throughout respiration. The

remaining inferior nodes attach to the ribs and intercostal muscles which undergo significant displacement during respiration. Respectively, rigid and non-rigid free form deformation (FFD) registrations were used to obtain the motion of the ribs and surrounding intercostal muscles intersecting with the diaphragm peripheral region from end exhalation to end inhalation. These displacements were then assigned to the nodes of the lower periphery of the diaphragm using a nearest a neighbor approach. Figure 3 shows the inferior regions on a diaphragm where boundary conditions are applied.

a)   b)
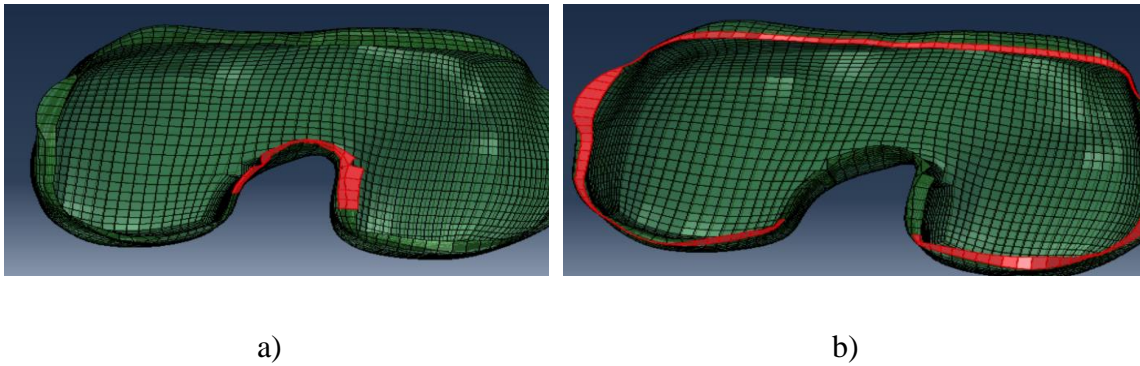
Fig. 3. The FE mesh is viewed inferiorly. Fixed boundary conditions are assigned to the inferior diaphragm highlighted in red a) and displacement boundary conditions assigned to peripheral regions highlighted in red b).

As indicated earlier, the loading in the diaphragm muscle is a result of muscle fiber contractions and is modelled based on an extension of the standard Hill's model for muscle[6,16]. Contraction forces in the diaphragm are simulated by applying prestresses incrementally to the rebar. Initially, predicting the contraction forces of the diaphragm was not considered to be sufficiently accurate because they are variable within a normal physiological range of approximately 200-300 kPa[32]. Furthermore, patients were elderly and some had lung and abdominal tumours tend to effect the functionality of their muscle[33]. As such, optimization was performed by simulating contraction until a best match was found between the contracted model's surface and the segmented contracted diaphragm surface. Contraction forces were assumed to be distributed uniformly throughout the muscle under normal healthy conditions. Peak vertical displacements in each hemi-diaphragm are measured by averaging the vertical displacement including the

uppermost nodes corresponding to each dome for each simulation. The predicted displacements are compared to fiducial displacements that correspond to each hemi-diaphragm dome from end exhalation to end inhalation.

3.2.3 Case Study: Unilateral Paralysis

As aforementioned, the model should be as adaptable as possible to each patient in order to most accurately capture the specific deformation field of their diaphragm. The model is inherently geometrically and mechanically adaptable. Another avenue to demonstrate the model's adaptability is to model a pathological diaphragm. Unilateral paralysis is selected for modelling due to its increased occurrence in individuals with lung cancer[34,35,36]. Although most cases of the disease are due to unknown causes, the development of tumours in the lung and esophagus have been associated to hemi diaphragm paralysis. The diaphragm is innervated by the left and right phrenic nerves[24]. Tumours that develop adjacent to these nerves can result in loss of signaling which ultimately leads to partial or no contraction of the affected side of the diaphragm. As the disease progresses, the affected side of the diaphragm is known to balloon into the lung which results in difficulty breathing. However, the body compensates by increasing the contraction forces in the remaining functional side of the diaphragm[36]. The irregular deformations patterns of the diaphragm and lung can easily be witnessed in 4D-CT scans of individuals with the condition. As a proof of concept, the geometry of a patient with unilateral paralysis is simulated by applying tensile forces to rebar in one half of a normal patient's diaphragm in order to simulate ballooning upward of the hemi diaphragm. This balloon occurs mainly along the axis of the muscle fibers because the presence of Z-discs, which are transversely oriented, are major structural components of the muscle tissue. Generally, the longer an individual has the disease the larger the migration of ballooning of the affected hemi-diaphragm occurs. After producing a new rest state geometry, the diaphragm contraction forces are then trained to differ in each half of the diaphragm. Simulation of unilateral paralysis is then performed by maintaining the forces in one half of the diaphragm whilst diminishing them in the other. The severity of

the disease is related to the extent of loss of contraction in the affected half of the diaphragm, a quantity that has not been determined by other groups. In this study the contraction forces in the left hemi-diaphragm were decreased by 25% in each case ranging from 75% to 0% of the contraction forces compared to the right hemi-diaphragm counterpart. This simulation study is performed for two purposes, firstly to simulate the deformation that occurs in a patient with such a condition, and secondly, if CT data was attained for a patient with the condition, the severity of the disease could also be potentially examined based on the predicted contraction forces and their discrepancies related to each hemi-diaphragm dome.

3.3 « Results »

Figure 4 a) shows the segmentation results of a single diaphragm muscle volume as a dark mass whilst overlaid with its corresponding 3D-CT image at end exhalation. Figure 4 b) shows the diaphragm muscle after being converted into a FE mesh. The region shown in red corresponds to approximately 143 cm^2 and represents the central tendon region of the muscle.
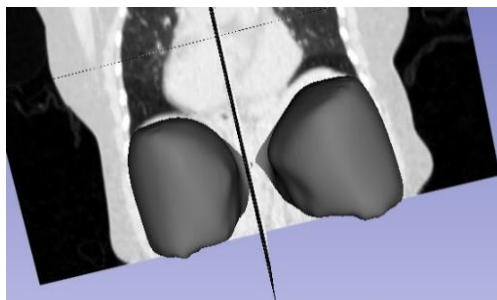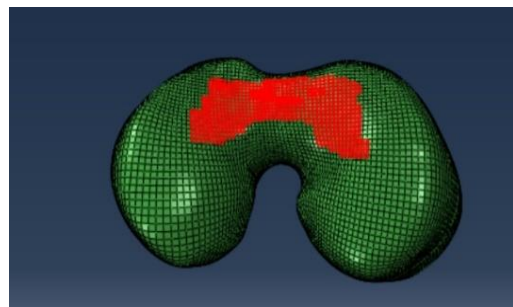
a)   b)

Fig. 4. a) shows a diaphragm segmentation overlaid with its corresponding CT images. b) shows a top view of the completed FE mesh with the assigned central tendon highlighted in red.

Figure 5 depicts the muscle fiber/rebar orientations for a single diaphragm model. Vectors are resolved for each element of the diaphragm model.
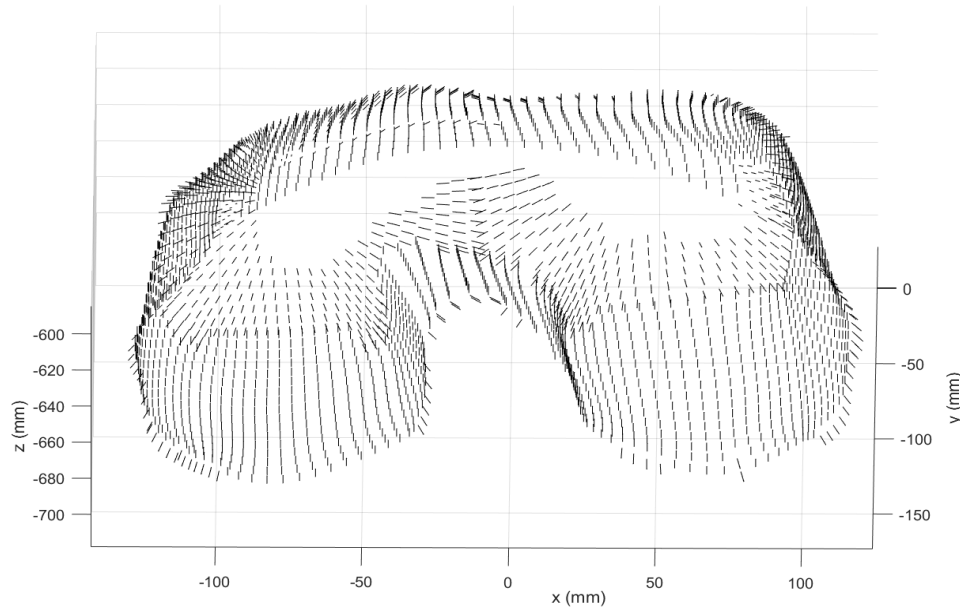
Fig. 5. Displays the muscle fiber orientations as a vector plotted for each element of the diaphragm.

Figure 6 a) depicts the segmentation results of the ribs and intercostal muscles in yellow overlaid with the corresponding diaphragm mesh nodes in blue.

After rigid and non-rigid registration of the ribs and intercostal muscles, respectively a deformation field was attained. The average displacement of the ribs and intercostals from end exhalation to end inhalation within a 1 cm radius for each lower peripheral diaphragm mesh node to be displacement was found to be sufficient to provide adequate information for the desired prescribed boundary conditions. Seen from a separate angle, Figure 6 b) shows the CT segmentation data that was used for determining the

displacements of the corresponding nodes to be displaced based on the predicted deformation field.
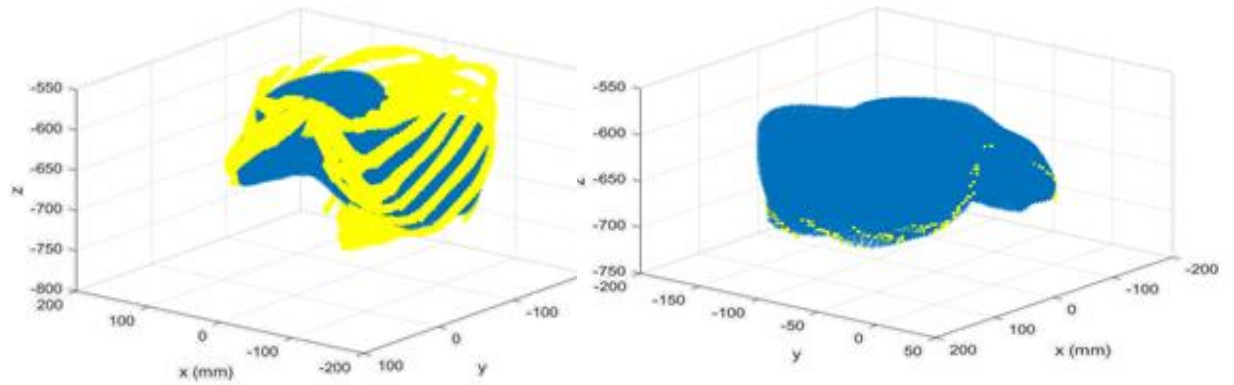
Fig. 6. a) Segmentation results of the ribs and intercostals are shown in yellow overlaid with the diaphragm mesh nodes in blue. The points associated with determining the lower displacement boundary conditions of the model based on the aforementioned registrations are shown in yellow dots relative to the diaphragm mesh nodes in blue b).

Figure 7 a) shows the model's predicted displacements at end inhalation for one of the patients. Displacements are shown in metres with maximal displacements predicted in the left and right hemidiaphragm domes. Figure 7 b) shows the comparison of the contracted diaphragm surfaces at end contraction where the model shown in red and CT segmentation in black, respectively. An iterative closest point (ICP) approach is used for comparison of the contracted models surface and the segmented diaphragm at end inhalation. The mean squared error using the ICP method converged to ~2.83 mm for the case shown in Figure 7 b). The contraction forces throughout the diaphragm that gave the most accurate result were optimized to approximately 250 kPa. Peak vertical displacement in the model were assessed and found to be 24.22 mm and corresponded to

the right hemidiaphragm dome, CT segmentations predicted 25.31 mm displacements in this region.

a)   b)
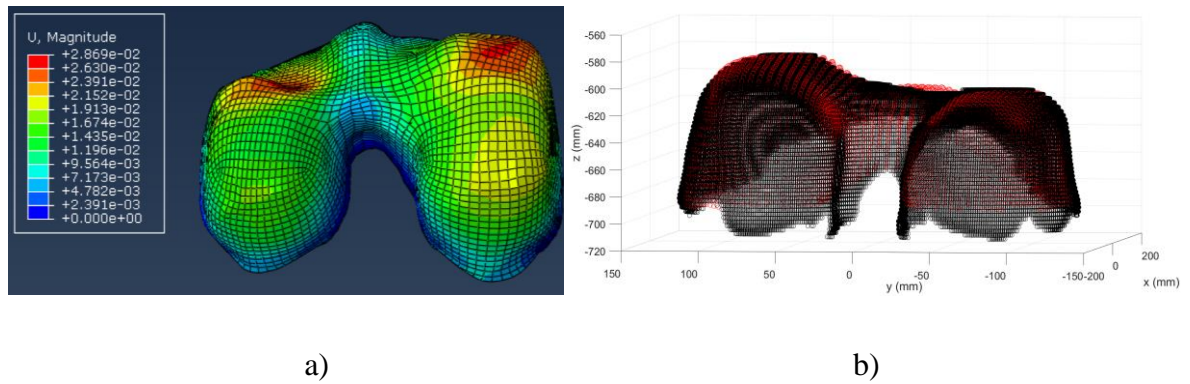
Fig. 7. The diaphragm displacements at end inhalation contraction are shown in a). The colour map displacements are displayed in metres which shows maximal values of ~2.87 cm. b) shows the overlaid contracted mesh surface in red scatter to the contract segmented diaphragm surface shown in black.

Figure 8 depicts the manually placed fiducials in the hemidiaphragm dome peaks. Fiducials were placed for each case corresponding to end exhalation and end inhalation phases. Overlaying both phases shows the before and after positions of the peaks as a result of muscle contraction. The differences calculated between the fiducials in the superior-inferior directions are indicative of the dome peak displacements.

Fig. 8. Shows fiducials that were placed manually on the hemi-diaphragm dome peaks for a set of patient 4D-CT data. Images corresponding to end exhalation and end

inhalation are shown overlaid. In some cases, multiple fiducials were placed in the
approximate peaks of each dome for both aforementioned phases.

Table 1 displays the values of the predicted contraction forces throughout each
diaphragm model. It also displays the ICP results and compares the models predicted and
segmentation predicted peak vertical displacements for each hemi-diaphragm dome.

Table 1. shows predicted contraction forces and calculated MSE values between
simulated and segmented contract diaphragm surfaces for each patient. Predicted and
calculated dome peak vertical displacements are shown for each hemi-diaphragm dome.

	Case 1	Case 2	Case 3
Contraction forces (kPa)	**~250**	**~266**	**~240**
MSE (mm)	**2.86**	**~3.21**	**~3.08**
Predicted Peak vertical displacement of left dome (mm)	**22.4**	**19.5**	**18.8**
Peak vertical displacement of fiducials of left dome (mm)	**21.3**	**17.8**	**18.0**
Predicted Peak vertical displacement of right dome (mm)	**24.2**	**21.1**	**17.9**
Peak vertical displacement of fiducials of right dome (mm)	**25.3**	**19.6**	**16.8**

3.3.1 Case Study: Unilateral Paralysis Results

Figure 8 a) shows a mesh generated from a single patient. Figure 8 b) shows the newly generated diaphragm geometry after inverting the contraction forces in the left hemi-diaphragm in order to simulate the "ballooning" affect of the pathological muscle.
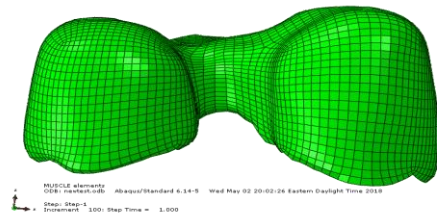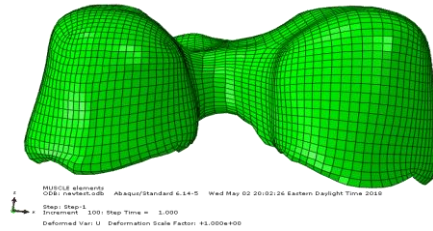
a)   b)

Fig. 9. The relaxed state geometry is shown in figure a) and figure b) shows the simulated pathological diaphragm rest state configuration. Note the slight elevation of the left hemi-diaphragm in panel b) compared to that of panel a).
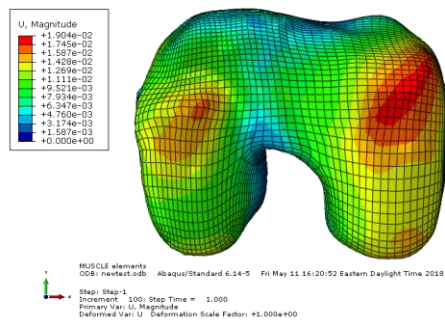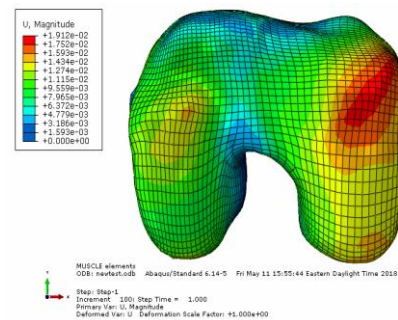
a)   b)
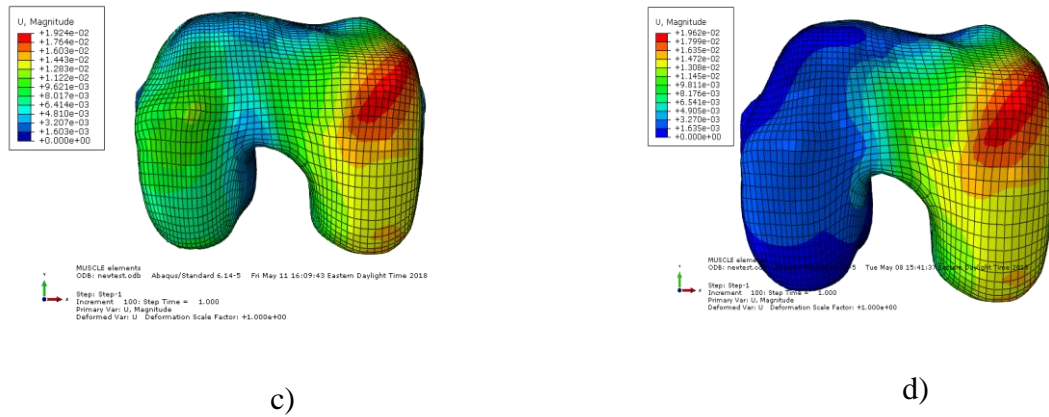
Fig. 10. Simulations were performed according to increasing severity of the disease. From a) to d) the contraction forces in the left hemi-diaphragm were decreased by 25% in each case ranging from 75% to 0% of the contraction forces compared to the right hemi-diaphragm counterpart.

3.4 « Discussion »

In order to simulate the diaphragm motion we modelled the diaphragm muscle using a continuum mechanics approach while considering muscle contractions and displacement boundary conditions. The Hill-type approach used captured transverse isotropy and used hyperelastic models to contract the modelled muscle tissue along the direction of muscle fiber installations at the resolution of the mesh elements. Mesh convergence analysis was performed using 3, 4, and 5 mm hexahedral elements in the diaphragm models and no tangible differences were seen. The motion produced was representative of physiological motion seen *in-vivo* for the diaphragm muscle. Our major focuses include validating the displacement fields produced by the model and to explore the adaptability of the model for normal and pathological diaphragms in addition to obtain an estimate of in vivo contraction forces generated in the diaphragm of lung cancer patients. The colourmap seen in Figure 7 a) shows that maximal displacements in the model coincide reasonably well with the apices of the left and right hemi-diaphragm domes, which agrees with *in vivo* behaviour. This agreement is further consolidated based on the MSE and peak

vertical displacement values presented in Table 1. One feature that should be included in the model is the aforementioned trans-diaphragmatic pressures related to the upper and lower diaphragm surfaces. Relatively small negative pressures are applied to the bottom surface of lung during inspiration while organs below the diaphragm generate a net positive pressure beneath the diaphragm surface[15].

The diaphragm muscle is not visible or easily accessible from outside the body, therefore studying the diaphragm and its deformations requires 3D medical images. The model geometries in this study were obtained using CT images. Satisfying 3D reconstructions of the diaphragm have been shown with similar results in both CT and MRI[7,37,38,39]. CT images generally have higher resolution and are more readily available, especially in conjunction with lung cancer treatment[38]. Algorithms for automatic and semi-automatic diaphragm segmentation are more readily available for CT images. Despite some contrast advantages of MRI, the contrast at the region of interest related to the lung-diaphragm interface is sufficiently high, aiding in both segmentation and validation.

The advent of hyperelasticity in our model is considered important because the diaphragm muscle undergoes large deformations during contraction while its tissue mechanics are intrinsically nonlinear. The model's mechanical characterizations were made based on a validated micro-to-macro mechanical approach for skeletal muscle tissue modelling. The model is therefore, adaptable to pathological conditions where tissue microstructural changes lead to mechanical alterations[40,41,42]. Incorporating stiffer Z-disk regions into the diaphragm FE model allowed for the capture of the transverse isotropy of skeletal muscle tissue as discovered in previous works. Our simulations assumed a uniform distribution of contraction forces throughout the diaphragm which is accurate for normal healthy breathing[43,24,35,34]. Furthermore, the act of rib cage expansion serves to elongate the muscle during contraction, which promotes isometric muscle contraction leading to a more consistent force output. The contraction forces we determined fell within the range of human physiological values[44]. It is noteworthy that the patients in this study were elderly and may have lung cancer, resulting in weakening of the diaphragm muscle. The diaphragm muscle thickness was assigned based on average measures for a human, however in reality there is variability in the muscle

thickness from patient to patient. For example, patients with chronic obstructive pulmonary disease (COPD) commonly experience diaphragm muscle thinning[20]. It is reasonable to expect that the predicted contraction forces in the diaphragm may have inaccuracies due to improper estimates of muscle thickness and muscle fiber content. Muscle fiber content in our model is related to the rebar to ECM ratio for the elements. Better imaging quality and processing would lead to more accurate patient specific measures for the muscle thickness, and morphometric analysis could aid in more accurately determining the myofiber to ECM content.

One major reason for the development of a diaphragm biomechanical model is to compensate for the potential inaccuracies of non-rigid registration of the diaphragm muscle. Low contrast CT images and non-physiologically based assumptions make diaphragm muscle registration difficult to perform and validate appropriately. The boundary conditions for our model, which more specifically are the prescribed boundary conditions at the inferior borders of the mesh, are done using registration. The rigid registration portion pertaining to the ribs could be considered a strength for our model because of the high rigidity of the ribs which facilitates accurate affine rib registrations used for determining such displacement boundary conditions. As such, it is anticipated that integrating the proposed model to a lung biomechanical model may potentially lead to a more reliable model for tumor motion prediction and consequently more favorable lung cancer EBRT outcome.

3.4.1 Case Study: Unilateral Paralysis

Pathologies such as hemi-diaphragm paralysis lead to a near loss of contraction in one half of the diaphragm and sometimes, increased contraction in the counterpart via natural compensation. The model was tuned to capture this condition to study the physical behaviour of the disease. This case study was considered for two main reason: to demonstrate the potential for patient specificity when building a model, and to aid in potential diagnosis of the disease. In its current state, the disease is difficult to diagnosis and is often done based on qualitative analysis using respiratory imaging techniques. We believe that our technique could not only model this pathology but also predict the

severity of the disease. Unilateral paralysis is often associated with the development of tumours that compensate the neural activation of the left or right phrenic nerve[35], so its diagnosis may be critical. In the future, attaining 4D-CT images of this disease would be of great interest to utilize for the development of a diaphragm biomechanical model.

3.5 « Conclusions »

A FEM for the simulation and quantification of diaphragm muscle motion was developed for the purpose that it may be used to enhance the accuracy of lung tumour tracking in EBRT. Further refinement and application of the model to numerous patients is ongoing to explore its efficacy. The model may prove useful for the incorporation into respiratory models to aid in diagnosis and treatment of diseases such as lung cancer. It may also be useful for diagnosis and treatment of cancers of other organs that are adjacent to the diaphragm (e.g. liver). The model may also be valuable in procedures such as attenuation correcting of the diaphragm for cardiac imaging. The model can be generated in a patient specific manner using 4D-CT images and its adaptability can serve for both normal and pathological diaphragms. Z-disk structures and a Hill's-type approach for skeletal muscle modelling capture the transversely isotropic and non-linear mechanics of the tissue and allow for simulation and estimation of the diaphragm contraction forces. Unilateral paralysis was simulated to further demonstrate the adaptability of the model and may prove useful for quantifying the severity of the disease, provided further testing is performed. Overall, the model has proven capable of simulating the physiological motion of the diaphragm muscle with discrepancies on the order of millimetres.

3.6 « References »

1. Fuerst B, Mansi T, Carnis F, et al. Patient-specific biomechanical model for the prediction of lung motion from 4-D CT images. *IEEE Trans Med Imaging*. 2015. doi:10.1109/TMI.2014.2363611

2. Karami E. A biomechanical approach for real-time tracking of lung tumors during

External Beam Radiation Therapy (EBRT). *Electron Thesis Diss Repos*. August 2017. https://ir.lib.uwo.ca/etd/4816. Accessed June 15, 2018.

3. Seyfi B, Santhanam AP, Ilegbusi OJ. A Biomechanical Model of Human Lung Deformation Utilizing Patient-Specific Elastic Property. *J Cancer Ther*. 2016. doi:10.4236/jct.2016.76043

4. Cervĩo LI, Chao AKY, Sandhu A, Jiang SB. The diaphragm as an anatomic surrogate for lung tumor motion. *Phys Med Biol*. 2009. doi:10.1088/0031-9155/54/11/017

5. Cerviño LI, Chao AKY, Sandhu A, Jiang SB. The diaphragm as an anatomic surrogate for lung tumor motion. *Phys Med Biol*. 2009;54(11):3529-3541. doi:10.1088/0031-9155/54/11/017

6. Zhang G, Chen X, Ohgi J, et al. Biomechanical simulation of thorax deformation using finite element approach. *Biomed Eng Online*. 2016. doi:10.1186/s12938-016-0132-y

7. Promayon E, Baconnier P. A 3D discrete model of the diaphragm and human trunk. August 2008. http://arxiv.org/abs/0808.0339. Accessed January 13, 2017.

8. Ladjal H, Saade J, Beuve M, Azencot J, Moreau J-M, Shariat B. 3D Biomechanical Modeling of the Human Diaphragm Based on CT Scan Images. In: Springer, Berlin, Heidelberg; 2013:2188-2191. doi:10.1007/978-3-642-29305-4_574

9. Pato MPM, Santos NJG, Areias P, et al. Finite element studies of the mechanical behaviour of the diaphragm in normal and pathological cases. *Comput Methods Biomech Biomed Engin*. 2011;14(6):505-513. doi:10.1080/10255842.2010.483683

10. Santos NJG. Preliminary Biomechanical Studies on the Diaphragmatic Function in Control and Patients with Loss of Motor Units. 2009. https://fenix.tecnico.ulisboa.pt/downloadFile/395139480394/resumo.pdf. Accessed August 2, 2017.

11. Troyer A De, Wilson TA. Action of the diaphragm on the rib cage. *J Appl Physiol*. 2016. doi:10.1152/japplphysiol.00268.2016

12. Farkas GA. Mechanical properties of respiratory muscles in primates. *Respir Physiol*. 1991. doi:10.1016/0034-5687(91)90038-K

13. Remmers JE. Inhibition of inspiratory activity by intercostal muscle afferents. *Respir Physiol*. 1970. doi:10.1016/0034-5687(70)90055-1

14. Pandy MG, Zajac FE, Sim E, Levine WS. An optimal control model for maximum-height human jumping. *J Biomech*. 1990. doi:10.1016/0021-9290(90)90376-E

15. Zhang G, Chen X, Ohgi J, et al. Biomechanical simulation of thorax deformation using finite element approach. *Biomed Eng Online*. 2016;15:18. doi:10.1186/s12938-016-0132-y

16. Pato MPM, Santos NJG, Areias P, et al. Finite element studies of the mechanical behaviour of the diaphragm in normal and pathological cases. 2010. doi:10.1080/10255842.2010.483683

17. Karami E, Wang Y, Gaede S, Lee T-Y, Samani A. Anatomy-based algorithm for automatic segmentation of human diaphragm in noncontrast computed tomography images. *J Med Imaging*. 2016. doi:10.1117/1.JMI.3.4.046004

18. Sieck GC, Gransee HM. Respiratory Muscles: Structure, Function, and Regulation. *Colloq Ser Integr Syst Physiol From Mol to Funct*. 2012;4(3):1-96. doi:10.4199/C00057ED1V01Y2012ISP034

19. Arora NS, Rochester DF. Effect of body weight and muscularity on human diaphragm muscle mass, thickness, and area.

20. Ladjal H, Shariat B, Azencot J, Beuve M. Appropriate biomechanics and kinematics modeling of the respiratory system: Human diaphragm and thorax. In: *2013 IEEE/RSJ International Conference on Intelligent Robots and Systems*. IEEE; 2013:2004-2009. doi:10.1109/IROS.2013.6696623

21. Saadé J, Didier A-L, Buttin R, et al. A PRELIMINARY STUDY FOR A BIOMECHANICAL MODEL OF THE RESPIRATORY SYSTEM.

22. Sieck GC, Ferreira LF, Reid MB, Mantilla CB. Mechanical properties of respiratory muscles. *Compr Physiol*. 2013. doi:10.1002/cphy.c130003

23. Polla B, D'Antona G, Bottinelli R, Reggiani C. Respiratory muscle fibres: specialisation and plasticity. *Thorax*. 2004;59(9):808-817. doi:10.1136/thx.2003.009894

24. CORDA M, VONEULER C, LENNERSTRAND G. PROPRIOCEPTIVE

INNERVATION OF THE DIAPHRAGM. *J Physiol*. 1965;178(1):161-177. http://www.ncbi.nlm.nih.gov/pubmed/14298107. Accessed January 12, 2018.

25. Gault ML, Willems MET. Aging, functional capacity and eccentric exercise training. *Aging Dis*. 2013;4(6):351-363. doi:10.14336/AD.2013.0400351

26. Hoppeler H, Luthi P, Claassen H, Weibel ER, Howald H. The ultrastructure of the normal human skeletal muscle. *Pflugers Arch Eur J Physiol*. 1973;344(3):217-232. doi:10.1007/BF00588462

27. Ogneva I V, Lebedev D V, Shenkman BS. Transversal stiffness and Young's modulus of single fibers from rat soleus muscle probed by atomic force microscopy. *Biophys J*. 2010;98(3):418-424. doi:10.1016/j.bpj.2009.10.028

28. Yoshikawa Y, Yasuike T, Yagi A, Yamada T. Transverse Elasticity of Myofibrils of Rabbit Skeletal Muscle Studied by Atomic Force Microscopy. *Biochem Biophys Res Commun*. 1999;256(1):13-19. doi:10.1006/bbrc.1999.0279

29. Wheatley BB, Odegard GM, Kaufman KR, Donahue TLH. How does tissue preparation affect skeletal muscle transverse isotropy? *J Biomech*. 2016;49(13):3056-3060. doi:10.1016/j.jbiomech.2016.06.034

30. Lieber RL, Runesson E, Einarsson F, Fridén J. Inferior mechanical properties of spastic muscle bundles due to hypertrophic but compromised extracellular matrix material. *Muscle Nerve*. 2003;28(4):464-471. doi:10.1002/mus.10446

31. Haddad SMH, Samani A. A novel micro-to-macro approach for cardiac tissue mechanics. *Comput Methods Biomech Biomed Engin*. 2017;20(2):215-229. doi:10.1080/10255842.2016.1214270

32. Rospars JP, Meyer-Vernet N. Force per cross-sectional area from molecules to muscles: A general property of biological motors. *R Soc Open Sci*. 2016. doi:10.1098/rsos.160313

33. Menshikova E V, Ritov VB, Fairfull L, Ferrell RE, Kelley DE, Goodpaster BH. Effects of exercise on mitochondrial content and function in aging human skeletal muscle. *J Gerontol A Biol Sci Med Sci*. 2006;61(6):534-540. http://www.ncbi.nlm.nih.gov/pubmed/16799133. Accessed May 29, 2017.

34. Choi M, Lee N, Kim A, et al. Evaluation of diaphragmatic motion in normal and diaphragmatic paralyzed dogs using m-mode ultrasonography. *Vet Radiol*

Ultrasound. 2014. doi:10.1111/vru.12126

35. Elefteriades J, Singh M, Tang P, et al. Unilateral diaphragm paralysis: Etiology, impact, and natural history. *J Cardiovasc Surg (Torino)*. 2008.

36. D. N, D. M, D. Y, N. D. Unilateral diaphragmatic paralysis: How far to investigate? *Respirology*. 2012.

37. Gauthier A, Verbanck S, Estenne M, Segebarth C, Macklem P, Others. Three-dimensional reconstruction of the in vivo human diaphragm shape at different lung volumes. *J Appl Physiol*. 1994. doi:10.1152/jappl.1994.76.2.495

38. Cluzel P, Similowski T, Chartrand-Lefebvre C, Zelter M, Derenne J-P, Grenier PA. Diaphragm and Chest Wall: Assessment of the Inspiratory Pump with MR Imaging—Preliminary Observations. *Radiology*. 2000. doi:10.1148/radiology.215.2.r00ma28574

39. Craighero S, Promayon E, Baconnier P, Lebas JF, Coulomb M. Dynamic echo-planar MR imaging of the diaphragm for a 3D dynamic analysis. *Eur Radiol*. 2005. doi:10.1007/s00330-004-2482-2

40. Mathur S, Brooks D, Carvalho CRF. Structural alterations of skeletal muscle in copd. *Front Physiol*. 2014;5:104. doi:10.3389/fphys.2014.00104

41. Orozco-Levi M, Gea J, Lloreta J, et al. Subcellular adaptation of the human diaphragm in chronic obstructive pulmonary disease. http://erj.ersjournals.com/content/erj/13/2/371.full.pdf. Accessed May 19, 2017.

42. Polla B, D 'antona G, Bottinelli R, Reggiani C. Respiratory muscle fibres: specialisation and plasticity. *Thorax*. 2004;59:808-817. doi:10.1136/thx.2003.009894

43. Pickering M, Jones JFX. The diaphragm: Two physiological muscles in one. *J Anat*. 2002. doi:10.1046/j.1469-7580.2002.00095.x

44. Rospars J-P, Meyer-Vernet N. Force per cross-sectional area from molecules to muscles: a general property of biological motors. *R Soc open Sci*. 2016;3(7):160313. doi:10.1098/rsos.160313

Chapter 4

4 « Summary, Conclusions, and Future Work»

4.1 « Summary»

The overall goal of this thesis was to develop a biomechanically accurate model of the human diaphragm muscle capable of accurately predicting its displacement and stress distribution throughout respiration. The purpose of the model is to gain insight into the muscle physiology, pathology, and potentially aid in diagnosis and treatment of respiratory related diseases. Two levels of biomechanical modelling pertaining to the diaphragm were tackled through the investigations presented in this thesis. The first involved developing a framework to characterize the intrinsic mechanical properties of the diaphragm skeletal muscle tissue based on its microstructure under normal and pathological conditions. The second level involved building patient specific models of the diaphragm muscle in healthy and diseased states.

4.2 « Chapter 2: A Micro to Macro Mechanical Approach for Skeletal Muscle Tissue Mechanical Characterization»

A novel approach for characterizing skeletal muscle tissue mechanics under normal and potential pathological conditions was proposed in this chapter. The major goal of this chapter was to capture the overall passive mechanics of skeletal muscle tissue geared towards the diaphragm muscle. Hyperelasticity and transverse isotropy were modelled through using rebars mimicking myofibers that are oriented within the tissue model in accordance with the known myofiber orientation in the diaphragm. The proposed model also captures the variable stiffness of the diaphragm across myofiber direction. This was accomplished by incorporating optimized Z-disk mechanics in the model. As seen in Chapter 1, the diaphragm is a skeletal muscle and has a sophisticated microstructure including various constituents such as myofibers, collagen fibers, mitochondria, fat, and Z-disks. The approach is based on the muscle tissue composition and organization of its microstrucutural components and their associated mechanics. The major parts that were

considered for the model's approach include: 1) the extracellular matrix (background tissue) including collagen, mitochondria, and fat; 2) the myofibril bundles, and 3) the Z-disk structures. The tissue constituents were chosen based on morphological studies available in the literature. Variations on the volume percentages and constituent mechanics were considered in accordance with physiology and pathology to determine the skeletal muscle tissue intrinsic mechanics. To achieve the proposed model, FE tissue samples were constructed for modelling of the background and whole tissue by distributing the tissue constituents throughout sample volumes with their associated mechanical properties. The FE models developed were used to simulate uniaxial tests to obtain related stress-strain data. The first step involved quantification of the skeletal muscle tissue constituents pertaining to the background (ECM) and myofiber bundles using hyperelastic fittings or parameters attained through literature review. The background tissue was modelled as a cylindrical specimen which underwent simulated uniaxial testing in order to characterize its overall behavior, using a Yeoh hyperelastic fitting. Next, a self-contained anisotropic hyperelastic composite model of the whole skeletal muscle tissue consisting of background, myofiber bundle, and Z-disk parts was constructed for simulated uniaxial testing along and across the myofiber directions. Z-disk structures were incorporated because of their known structural rigidity where their micro mechanics were optimized such that the whole tissue mechanics were found to best match the overall transversely isotropic mechanics of the whole tissue, according to experimental data in the literature.

The approach was applied for normal skeletal muscle tissue in order to model the stress-strain relationship along and across fiber directions in order to give good agreement to experimental trends reported in the literature. A sensitivity analysis was developed and performed to assess variations in the tissue stress-strain relationship related to the volume percentages of each constituent. As predicted, the tissue is most sensitive to volumetric changes with respect to collagen. Pathological changes were also considered with respect to micro mechanical alterations of constituents such as the myofiber bundles. This sought insight into the importance of morphometric analysis and characterization of the micro mechanics of tissue constituents. The FE muscle tissue model mechanics were compared to an existing transversely isotropic hyperelastic mathematical model in order to generate parameters specific to our model's mechanical behavior along and across fiber directions.

Overall, Chapter 2 was an important step towards the next phase of the project which required appropriate mechanical modelling of the diaphragm skeletal muscle tissue.

4.3 « Chapter 3: Micromechanics Based Modelling of in-vivo Respiratory Motion of the Diaphragm Muscle »

In this chapter, a biomechanical model for the human diaphragm muscle was presented. Semi-automatic segmentation of 4D-CT images at end exhalation was performed for diaphragm muscles of three patient selected randomly. They were then converted into thin FE meshes to achieve each patient specific diaphragm geometry. A relatively stiff central tendon region was defined according to the literature. The model's mechanics was devised based on a micro to macro mechanical approach for skeletal muscle tissue. A Hill's model type composite material approach was used which included background tissue (ECM), reinforcement rebars (myofiber bundles), and Z-disk regions. The two major parts of the Hill's-type material model include the mechanically active/passive myofibril part and the passive background part. The myofibers were distributed throughout the elements of the FE model of the diaphragm such that their directions were consistent with the fibrous structure of the diaphragm anatomy based on a radial pattern presented in the literature. The model's boundary conditions were fixed at the spine and were also based on rigid and non-rigid image registrations of the patients ribs and intercostal muscles intersecting with the diaphragm, respectively. Image registrations were performed from end exhalation to end inhalation and displacements boundary conditions were applied to the inferior borders of the diaphragm to capture rib cage expansion. The transversely isotropic hyperelastic model was implemented using nonlinear FE analysis. Prestresses were applied incrementally to rebars in order to simulate muscular contraction and the contraction forces applied were optimized such that the contracted model's configuration best matched the corresponding segmentation of the 4D-CT image at end inhalation. The predicted contraction forces fell within possible physiological values. The performance of the model was assessed based on an iterative closest point approach in order to compare the model's contracted surface to its observed counterpart obtained through segmenting the diaphragm in the contracted configuration. Displacements of a set of anatomical fiducials were also

evaluated for each hemi-diaphragm dome and compared to their counterparts in the manually segmented diaphragm surfaces. Overall, the physiological motion showed good qualitative and quantitative agreement with normal *in-vivo* behavior. The diaphragm was considered under the pathological condition of unilateral paralysis for the interest of potential future works, aid in diagnosis, and demonstration of the adaptability of the model to potential unilateral paralysis patients.

4.4 « Conclusions and Future Directions»

Results presented in this thesis indicate that the biomechanical model of the diaphragm developed was capable of simulating the physiological motion seen during *in-vivo* respiration. The adaptability of the muscle tissue modelling, and diaphragm model also promote their utility towards characterizing skeletal muscle tissue and the potential for patient specific modelling. The results are encouraging, only three patient specific diaphragm models were developed making the sensitivity of the model to anatomical changes difficult to assess. Some key points that would lead to improvements of the model include: 1) improved segmentation techniques allowing for more geometrically accurate patient specific models and improved validation; 2) improved morphometric analysis techniques in order to better characterize the muscle tissue mechanics based on its composition; 3) increasing the resolution of the meshes in order to more finely resolve muscle fiber installations, and 4) better understanding the anatomy and physiology of the diaphragm muscle. In the future, applying our model to more patients including patients with unilateral paralysis would be of great interest to further assess the robustness of the model. Incorporating this model into respiratory models would also be of interest as it has a good potential to assist in simulating respiration allowing for further insight into diagnosis and the potential for aid in treatment of respiratory diseases such as lung cancer.

Curriculum Vitae

Name: Brett Coelho

**Post-secondary
Education and
Degrees:**

2010/9 - 2014/4   **Bachelor's Degree** (Bachelor of Medical Sciences Honors; Medical Biophysics) Degree status: Completed with Dean's honors list designation. Western University, London Ontario

**Honours and
Awards:**

2017/18   Queen Elizabeth II Graduate Scholarship in Science and Technology

2013/12   Dr. G. E. Hall Scholarships
                             500 (Canadian dollar) University of Western Ontario
                             Prize/Award.

2013/12   Alan C. Burton Course Prize in Medical Biophysics
                             500 (Canadian dollar) University of Western Ontario
                             Prize/Award Achieving the highest average in five medical biophysics core courses.

**Related Work
Experience:**

2016/9 – 2018/4   **Teaching Assistant**
                             Biomedical Engineering, Biophysics/Western University, University of Western Ontario: Biomechanics, Organic Chemistry, and Mechatronics Design Course.

2012/1 - 2013/4   **Research Assistant**
                             Medical Biophysics, University of Western Ontario
                             Part-time: Mixing and forming prostate and tumor phantoms for tumor detection analysis. Performing ultrasound and image processing.

Publications:

1. **Brett N. Coelho**, Elham Karami, Seyyed Mohammad Hassan Haddad, Western Univ. (Canada); Behzad Seify, Amirkabir Univ. of Technology (Iran, Islamic Republic of); Abbas Samani, Western Univ. (Canada). (2016). A biomechanical approach for in vivo diaphragm muscle motion prediction during normal

respiration. SPIE medical imaging. SPIE medical imaging: Image-Guided Procedures, Robotic Interventions, and Modeling, Conference Date: 2017/2 First Listed Author, Number of Contributors: 5.

2. **Brett N. Coelho**, Abbas Samani, Western Univ. (Canada). Micromechanics Based Modelling of in-vivo Respiratory Motion of the Diaphragm Muscle with the Incorporation of Optimized Z-disks Mechanics. SPIE medical imaging. SPIE medical imaging: Image-Guided Procedures, Robotic Interventions, and Modeling, Conference Date: 2018/3 First Listed Author, Number of Contributors: 2.